Energy Storage Materials 10 (2018) 139–159

Contents lists available at ScienceDirect

Energy Storage Materials

journal homepage: www.elsevier.com/locate/ensm

Mechanisms and properties of ion-transport in inorganic solid electrolytes

Bingkai Zhang[a], Rui Tan[a], Luyi Yang[a], Jiaxin Zheng[a], Kecheng Zhang[a], Sijia Mo[a], Zhan Lin[b,*], Feng Pan[a,*]

[a] School of Advanced Materials, Peking University Shenzhen Graduate School, Shenzhen 518055, People's Republic of China
[b] College of Chemical and Biological Engineering, Zhejiang University, Hangzhou 310058, People's Republic of China

ARTICLE INFO

Keywords:
All-solid-state lithium battery
Inorganic solid electrolyte
Ionic conductivity
Ion-transport mechanism
Structure stability
Interface stability

ABSTRACT

Compared with conventional lithium-ion batteries, all-solid-state lithium batteries (ASSLBs) based on inorganic solid electrolytes (ISEs) are relatively new research hotspots, which can overcome tough challenges in conventional lithium-ion batteries, such as potential combustion accidents resulted from flammable liquid electrolyte solvent, low energy density, and fussy manufacturing process. In this review, we focus on the ionic conductivity and stability of ISEs by discussing defect chemistry, ion-doping or elemental substitution, ion-transport mechanism, phase stability, and interfacial stability in representative ISEs (e.g., LISICON-like, NASICON-like, perovskite/anti-perovskite, and garnet electrolytes). The general illustration of structures and fundamental features being important to ionic conductivity or stability are examined, including ion occupancies, ion migration paths and dimensionalities, carrier types, point defects, ion-doping sites, and interfacial structures. Experimental and theoretical studies are discussed in parallel to give a deep and comprehensive understanding on ion transport, ion doping, and stability in ISEs. The common features of Li-ion transport mechanism and several possible research directions are also suggested for facilitating further improvement on the ASSLBs performance. We believe this review will contribute to the deep understanding on the ionic conductivity and stability of ISEs and help for further development of advanced ISEs in the field.

1. Introduction

All-solid-state lithium batteries hold the promise of providing energy storage with high safety and high specific energy, making them ideal candidates for use in electronics, automobiles, and stationary power stations [1–3]. Compared to conventional liquid electrolyte-based lithium-ion (Li-ion) batteries, the most distinctive feature for ASSLBs is the adoption of inorganic solid electrolytes (ISEs), which enhance their safety and stability (Fig. 1a and b) [4]. There are some inherent advantages in using ISEs for rechargeable batteries: (i) high Li-ion transference number (~ 1) at room temperature; (ii) good electrochemical stability and wide electrochemical window; (iii) amenable to inexpensive and environmentally friendly thin-film synthesis technique; (iv) suitability to some electrodes that cannot coexist with liquid electrolyte [5,6].

Until now, low ionic conductivities at ambient temperature and poor stabilities for ISEs have plagued commercial applications of ASSLBs. The ionic conductivities of most ISEs are inferior to those of organic liquid electrolytes at room temperature (~ 10 mS cm^{-1}) (Fig. 1c). Many ISEs are unstable at low potentials against negative electrodes such as graphite and metallic lithium anodes, while some ISEs are reactive towards cathode materials, resulting in high interfacial resistance [6]. Therefore, the optimization and discovery of ISEs with high ionic conductivities and high stabilities are critical to the application of ASSLBs, which depend on a better understanding of fundamental science in ISEs.

Recently, the synergy between experimental and computational studies on Li-ion battery materials has been widely adopted. Although lots of experiments have been carried out on the synthesis-structure-property correlation for various ISEs, there are still many key scientific issues such as ion-transport mechanism left due to technological limit, time consumption, and cost. Computational methods now play a vital role in characterizing and predicting the structures and properties of complex materials at atomic scale. Usually, the exchange of ideas and results between experimental and theoretical studies is mutually beneficial. Computational chemistry methods such as density functional theory (DFT), molecular dynamics (MD), and Monte Carlo (MC) method have been proven useful regarding to the chemistry of battery materials.

In this review, we first introduce the experimental and theoretical methods to study ionic conductivity and interfacial stability in the

* Corresponding authors.
E-mail addresses: zhangbk@pkusz.edu.cn (B. Zhang), tanrui@sz.pku.edu.cn (R. Tan), yangly@pkusz.edu.cn (L. Yang), zhengjx@pkusz.edu.cn (J. Zheng), 1601213911@sz.pku.edu.cn (K. Zhang), 1601213897@sz.pku.edu.cn (S. Mo), 0013131@zju.edu.cn (Z. Lin), panfeng@pkusz.edu.cn (F. Pan).

http://dx.doi.org/10.1016/j.ensm.2017.08.015
Received 21 February 2017; Received in revised form 30 August 2017; Accepted 30 August 2017
Available online 06 September 2017

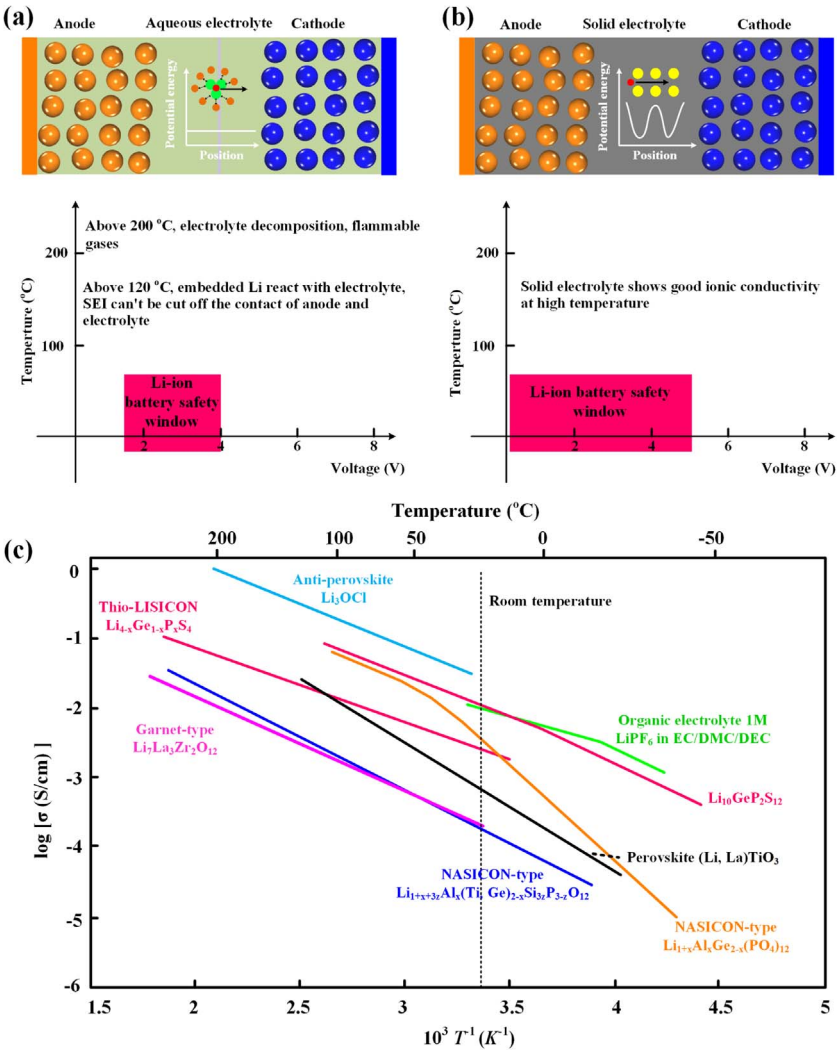

Fig. 1. Schematic representation of (a) conventional organic liquid lithium-ion battery and (b) all-solid-state lithium-ion battery. (c) Reported total ionic conductivity as a functional of temperature for different electrolytes [84], the data of anti-perovskite from Ref. [82].

Supporting information (SI). The abbreviations in this review is list in Table 1. Then, we review the progresses on ionic conductivity properties for four kinds of representative ISEs, i.e., LISICON-like (lithium superionic conductor), NASICON-like (sodium superionic conductor), perovskite/anti-perovskite and garnet electrolytes, by analyzing point defects, structures, ion-transport mechanisms, and methods to improve ionic conductivity. Reported Li-ion conductivities and lattice parameters of representative ISEs are summarized in Table 2. Next, we review phase stability and interface stability, including interfaces between ISEs and anodes or cathodes. Last but not least, we provide conclusions and perspectives on future development for advanced ISEs. In addition, in this review we focus on more recent studies and those with a tie to the nature of crystal structures, defects, ion-transport mechanisms, and phase/interface stabilities in ISEs.

2. Ionic conductivity: defect and ion-transport mechanism

The ionic conductivity is strongly correlated with defects of crystal structures. Defect includes many types, such as point defects, line defects, planar defects, volume defects, and electron defects. Among them, point defects with associated properties play an important role in ion-transport mechanism in a crystal. The illustration of different point defect models are shown in Fig. 2a. Point defects widely exist in ISEs, and they can be intrinsic or stoichiometric. Typical point defects are Frenkel defects (the defects are vacancies accompanied by an interstitial ion) and Schottky defects (the defects are anion vacancies accompanied by a cation vacancy). For a given ISE, point defects decide the type and concentration of carriers, that is, point defects directly influence the ionic conductivity of ISEs. The crystal structure of ISEs includes spatial arrangement of immobile ions, the structure of immobile framework and the Li-ion sublattice. The interaction between Li-ions and immobile framework has great effects on the Li-ion mobility (Fig. 2b and c). The spatial arrangements and structures of immobile ions or framework affect Li-ion migration path and dimensionality.

2.1. Defect chemistry

The defect chemistry of ISEs is the first step to understand their ion-transport mechanism. Point defects, such as Schottky, Frenkel, and antisite disorder, determine the Li-ion conductivity of ISEs [7,8]. Furthermore, charged point defects can also associate to form localized clusters, which have significant effects on ion-transport behavior. Therefore, the formation energy $\Delta H_{d,q}$ of a defect d in charge state q is calculated from the equation:

$$\Delta H_{d,q}(E_F, \{\mu_i\}) = E_{d,q} - E_0 - \sum_i n_i\mu_i + q(E_V + E_F) \quad (1)$$

where $E_{d,q}$ is the total energy of supercell with defect d in charge state q, E_0 is the total energy of the pristine supercell, and μ_i and n_i are the

Table 1.
List of abbreviations.

ASSLBs	All-solid-state lithium batteries	TEM	Transmission electron microscopy
ISEs	Inorganic solid electrolytes	LLTO	$Li_{3x}La_{2/3-x}TiO_3$
LISICON	Lithium superionic conductor	LLZO	$Li_7La_3Zr_2O_{12}$
NASICON	Sodium superionic conductor	LALZO	$Li_{7-3x}Al_xLa_3Zr_2O_{12}$
DFT	Density functional theory	LGPS	$Li_{10}GeP_2S_{12}$
AIMD	*Ab initio* molecular dynamics	LXPS	$Li_{10}XP_2S_{12}$ (X = Si, Ge, Sn)
MD	Molecular dynamics	LMPX	$Li_{10\pm1}MP_2X_{12}$ (M = Ge, Si, Sn, Al, or P, and X = O, S, Se)
MC	Monte carlo	LSPSCl	$Li_{9.54}Si_{1.74}P_{1.44}S_{11.7}Cl_{0.3}$
MSD	Mean square displacement	LGP	$LiGe_2(PO_4)_3$
BV	Bond valence	LTP	$LiTi_2(PO_4)_3$
NEB	Nudged elastic band	LATP	$Li_{1+x}Al_xTi_{2-x}(PO_4)_3$
EIS	Electrochemical impedance spectroscopy	LAGP	$Li_{1+x}Al_xGe_{2-x}(PO_4)_3$
GB	Grain boundary	SCL	Space charge layer
ALD	Atomic layer deposition	LiRAP	Lithium-rich anti-perovskite
DC	Direct current	c-LLZO	Cubic-LLZO
NPD	Neutron powder diffraction	t-LLZO	Tetragonal-LLZO
NMR	Nuclear magnetic resonance	LLZTO	$Li_{6.4}La_3Zr_{1.4}Ta_{0.6}O_{12}$
EMPA	Electron microprobe analysis	LLBZT	$Li_{6.5}La_{3-x}Ba_xZr_{1.5-x}Ta_{0.5+x}O_{12}$
AES	Auger electron spectroscopy	LBLTO	$Li_{5+x}Ba_xLa_{3-x}Ta_2O_{12}$
XRD	X-ray diffraction	LGLZSO	$Li_{6.55+y}Ga_{0.15}La_3Zr_{2-y}Sc_yO_{12}$
MEM	Maximum-entropy method	LNMO	$LiNi_{0.5}Mn_{1.5}O_4$
MAS NMR	Magic angle spinning NMR	LATSPO	$Li_{1+x+y}AlyTi_{2-y}SixP_{3-x}O_{12}$
SLR	Spin-lattice relaxation	LCO	$LiCoO_2$
LSV	Linear sweep voltammetry	LNO	$LiNbO_3$
STEM	Scanning transmission electron microscopy	LMO	$LiMnO_2$
STEM/EELS	STEM coupled with electron energy loss spectroscopy	LFP	$LiFePO_4$
XPS	X-ray photoelectron spectroscopy	μ_{Li}	Li chemical potential
EDX	Energy dispersive X-ray analysis	MCI	Mixed ionic/electronic conducting interphase
TEM	Transmission electron microscopy	SEI	solid electrolyte interphase

Table 2.
Reported ionic conductivities and lattice parameters of inorganic solid electrolytes including LISICON-like, NASICON-like, perovskite, and garnet.

Classification	Ionic conductivity (S/cm)	Temperature (K)	Lattice parameters (Å)			Space group	Ref.
			a	b	c		
LISICON-like							
$Li_7P_3S_{11}$	3.20×10^{-3}	298	12.48	6.03	12.50	*P*-1	[201]
β-Li_3PS_4	3.0×10^{-2}	500	12.82	8.22	6.12	*Pnma*	[202,203]
$Li_{9.6}P_3S_{12}$	1.00×10^{-2}	298	8.71	8.71	12.47	*P42/nmc*	[18]
$Li_{10}GeP_2S_{12}$	1.20×10^{-2}	298	8.69	8.69	12.60	*P42/nmc*	[32]
$Li_{3.25}Ge_{0.25}P_{0.75}S_4$	2.20×10^{-3}	298	13.40	7.66	6.07	*P42/nmc*	[204]
$Li_{3.4}Si_{0.4}P_{0.6}S_4$	6.4×10^{-4}	298	13.37	7.88	6.11	*P42/nmc*	[205]
$Li_{9.54}Si_{1.74}P_{1.44}S_{11.7}Cl_{0.3}$	2.50×10^{-2}	298	8.71	8.71	12.57	*P42/nmc*	[43]
NASICON-like							
$LiTi_2(PO_4)_3$	3.83×10^{-7}	298	8.51	8.51	20.85	*R-3c*	[206]
$Li_{1.3}Al_{0.3}Ti_{1.7}(PO_4)_3$	3.00×10^{-3}	298	8.50	8.50	20.82	*R-3c*	[56]
$Li_{1.2}Ti_{1.8}Sc_{0.2}(PO_4)_3$	2.5×10^{-3}	298	8.53	8.53	20.92	*R-3c*	[51]
$Li_{1.6}Al_{0.6}Ge_{0.8}(PO4)_3$	0.70×10^{-3}	298	8.38	8.38	20.64	*R-3c*	[50]
$Li_{1.3}Al_{0.3}Ti_{1.7}(PO_4)_3$	1.21×10^{-3}	298	8.51	8.51	20.83	*R-3c*	[63]
$Li_{1.4}Al_{0.4}Ti_{1.6}(PO_4)_3$	5.63×10^{-3}	298	8.50	8.50	20.79	*R-3c*	[66]
$Li_{1.3}Al_{0.3}Ti_{1.7}(PO_4)_3$	6.20×10^{-3}	298	8.49	8.49	20.86	*R-3c*	[54]
Pervoskite							
$La_{0.57}Li_{0.29}TiO_3$	1.60×10^{-3}	300	7.74	7.74	7.79	*Cmmm*	[87]
Li_3OCl	0.85×10^{-3}	298	3.91	3.91	3.91	*Pm3m*	[101]
$Li_3OCl_{0.5}Br_{0.5}$	1.94×10^{-3}	298	–	–	–	*Pm3m*	[101]
Li_2OHCl	2.8×10^{-3}	468	–	–	–	*Pm3m*	[109]
Garnet							
$Li_7La_3Zr_2O_{12}$	1.63×10^{-6}	298	13.13	13.13	12.66	$I4_1/acd$	[207]
$Li_7La_3Zr_2O_{12}$	3.10×10^{-4}	298	12.97	12.97	12.97	*Ia-3d*	[124]
$Li_7La_3Zr_2O_{12}$	5.11×10^{-4}	298	12.97	12.97	12.97	*Ia-3d*	[208]
$Li_{6.55}La_3Zr_2Ga_{0.15\sim0.3}O_{12}$	1.30×10^{-3}	298	12.98	12.98	12.98	*Ia-3d*	[117,209]
$Li_7La_3Zr_2O_{12}$ (0.9 wt% Al)	3.55×10^{-4}	298	12.97	12.97	12.97	*Ia-3d*	[30]
$Li_{6.4}La_3Zr_{1.4}Ta_{0.6}O_{12}$	1.00×10^{-3}	298	12.92	12.92	12.92	*Ia-3d*	[13]
$Li_{6.5}La_3Zr_{1.75}Te_{0.25}O_{12}$	1.02×10^{-3}	303	12.91	12.91	12.91	*Ia-3d*	[210]
$Li_{7.06}La_3Zr_{1.94}Y_{0.06}O_{12}$	9.56×10^{-4}	298	12.97	12.97	12.97	*Ia-3d*	[211]
$Li_{6.5}La_{2.9}Ba_{0.1}Zr_{1.4}Ta_{0.6}O_{12}$	8.30×10^{-4}	300	12.94	12.94	12.94	*Ia-3d*	[116]
$Li_{6.5}La_3Zr_{1.5}Ta_{0.5}O_{12}$	7.94×10^{-4}	300	12.95	12.95	12.95	*Ia-3d*	[116]
$Li_{6.4}La_3Zr_{1.7}W_{0.3}O_{12}$	7.89×10^{-4}	303	12.97	12.97	12.97	*Ia-3d*	[212]
$Li_{6.6}La_3Zr_{1.6}Sb_{0.4}O_{12}$	7.70×10^{-4}	303	12.96	12.96	12.96	*Ia-3d*	[213]

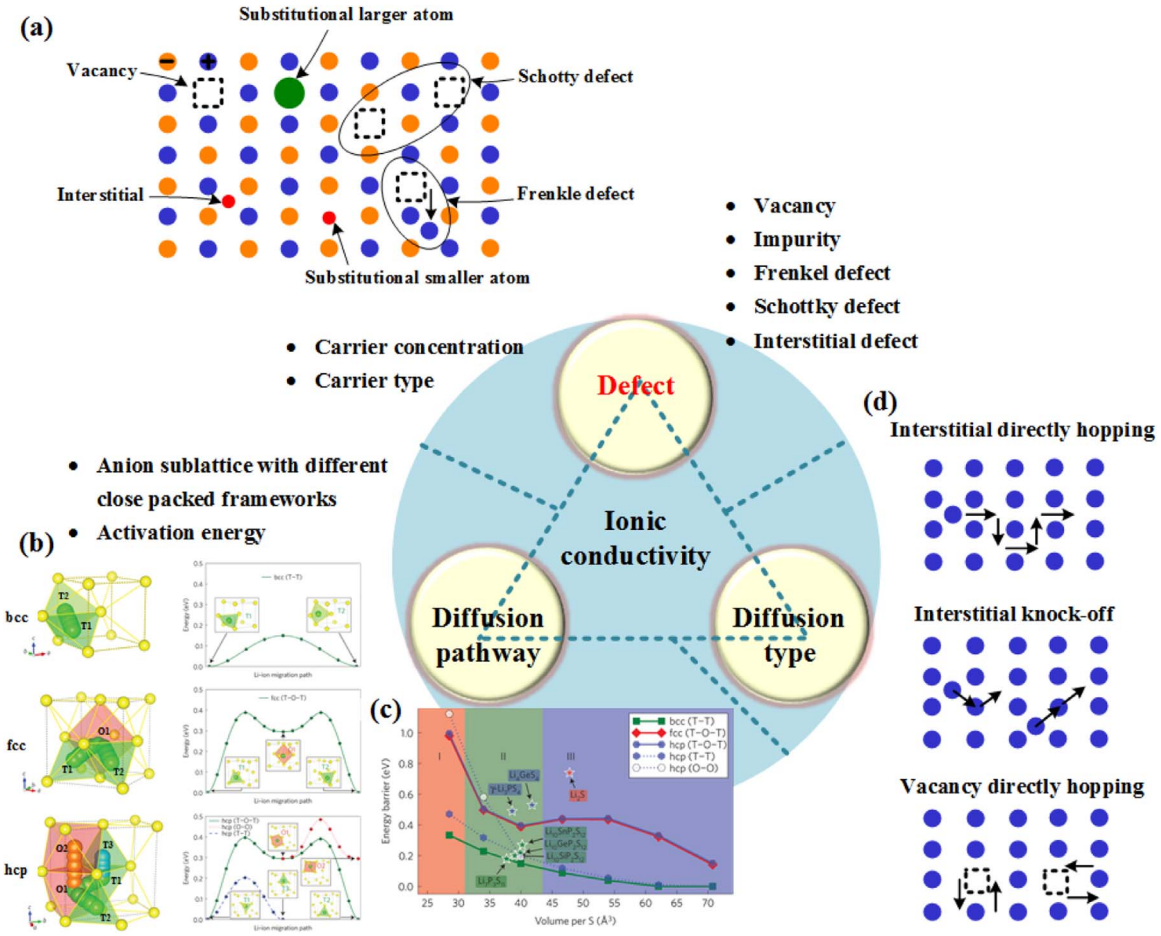

Fig. 2. Schematic representation of the defect, migration pathway, and migration mechanism in ISEs. The figures in (b) and (c) are from Ref. [12].

chemical potential of the atomic species of the i_{th} defect and the corresponding number of atoms added to or removed from the structure. E_V and E_F is the valence band maximum in the bulk and the Fermi level relative to the E_V, respectively. In the case of a vacancy defect (i.e., a removed atom), the sign of the n_i is negative. On the other hand, if the defect is an interstitial (i.e., an added atom), this sign is positive.

Point defects in ISEs may occur under the following conditions. i) When fraction occupying ratio of ion sites exists in ISEs, which leads to many vacancies in ISEs. Almost all of ISEs have fraction sites. In β-Li_3PS_4, the 4c and 4b sites for Li-ion are 32% and 68% occupied, respectively. In LGPS ISE, 8f and 16h sites for Li-ion are 64% and 69% occupied, respectively. In perovskite $Li_{3x}La_{2/3-x}TiO_3$ (LLTO), the only two-thirds of A sites are occupied by La-ion. In garnet $Li_7La_3Zr_2O_{12}$ (LLZO), the tetrahedral (24d) and octahedral sites (48g) for Li-ion are 80% and 40% occupied, respectively. Shi and Wang et al. [9] studied the Li-associated defect thermodynamics of Li_3PS_4. The thermodynamics of different defects were analyzed, and the dominant carriers were determined over a voltage of 0–5 V vs. Li/Li^+. The dominant diffusion carrier type in Li_3PS_4 varied from single Li_i^+ to coupling Li_i^+ and V_{Li}^- with the rising of applied voltage. Therefore, the disordered Li-ion sublattice provide medium Li/vacancy or Li/interstitial ratio to help Li-ion motion. ii) When element doping or substitution exits in ISEs, which can cause various point defects in ISEs. Element doping or substitution in ISEs optimize conductivity or other perperties. For example, doping Sr^{2+} at La^{3+} sites in LLZO, the defect reaction follows the form: $2SrO + 2La_{La}^{\times} + Li_2O + 2\square \rightarrow 2Sr'_{La} + 2Li^{\bullet} + La_2O_3$. Superscripts indicate the net charge (Neutral, $^{\times}$; positive, $^{\bullet}$; or negative, $'$). Therefore, there are Sr'_{La} and interstitial Li-ion defects in LLZO. This part will be detailedly discussed in the following section. iii) When ISEs are under extreme conditions (such as low oxygen partial pressure), electrode potential (or Li chemical potential) and charging-discharging process in ASSLBs, ISEs may occur defect reaction. Considering the effect of electrode potential, Shi et al. [10,11] explored defect thermodynamics and associated diffusion mechanisms in crystalline Li_2CO_3. They showed that Li-ion interstitials (Li_i^+) were dominant diffusion carriers when applied voltage below 0.98 V, while Li-ion vacancies became the dominant diffusion carriers when applied voltage above 3.98 V. The interstitial Li_i^+ diffused through a knock-off mechanism by continuously displacing Li-ions in neighboring sites. In addition, the Ti^{4+} in $LiTi_2(PO_4)_3$ and LLTO is reduced by Li-metal under high Li chemical potential, which bring Ti'_{Ti} in ISEs.

2.2. Structures, ion-transport mechanisms and methods to improve ionic conductivity

For ASSLBs, the Li-ion transport within ISEs' crystals is an important process for overall charge-transfer reaction. Three factors such as carrier type, diffusion pathway, and diffusion type, govern Li-ion transport mechanism within superionic ISEs. Carrier type is closely linked to defect chemistry as introduced in Section 3.1. Diffusion pathway is greatly correlated with anion arrangement. Wang et al. [12] highlighted this correlation and suggested anion sublattice with bcc-like frameworks with a low energy barrier was more favorable for Li-ion diffusion than in other close packed frameworks (Fig. 3c and d). The Li-ion diffusion type also affects ionic conductivity and three types (interstitial directly hopping, interstitial knock-off, and vacancy directly hopping) are outlined in Fig. 2d. An understanding of the ion-transport mechanism in ISEs is crucial to optimize and design ISEs with high ionic conductivities. In the following section, we present previous

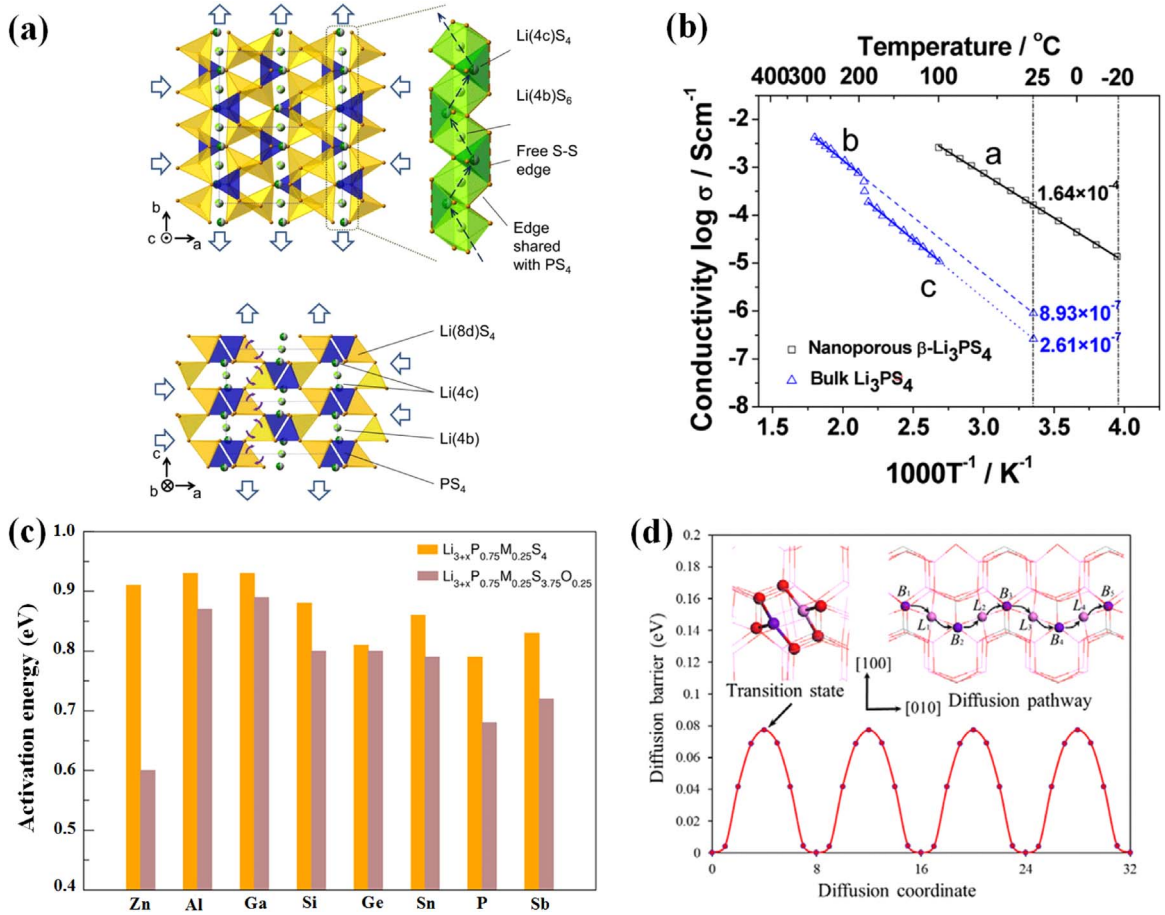

Fig. 3. (a) Crystal structure for β-Li_3PS_4 [222]. (b) Arrhenius plots for nanoporous β-Li_3PS_4 (line a), bulk β-Li_3PS_4 (line b), and bulk γ-Li_3PS_4 (line c) [19]. (c) Li-ion migration activation energy for β-Li_3PS_4 and its doping derivatives by force-based BV method [23]. (d) Schematic representation of knock-off mechanism in β-Li_3PS_4 [19].

experimental and computational studies on Li-ion transport mechanisms of four typical ISEs: LISICON-like, NASICON-like, perovskite/anti-perovskite, and garnet electrolytes.

2.2.1. *LISICON-like*

The LISICON-like (lithium super ionic conductor) material with the γ-Li_3PO_4-type framework structure, $Li_xM_{1-y}M'_yS_4$ (M = Si and Ge and M′ = P, Al, Zn, Ga, and Sb), was proposed by Hong et al. [13–16] In this family, lithium thiophosphate, Li_3PS_4, has been considered as one of the most promising compounds [17]. Kanno et al. [18] found that Li_3PS_4 gone through three transitions (γ → β → α) with the increase of temperature in the experimental, and ionic conduction was related to the PS_4 tetrahedron arrangement which affects the positions of Li-ions. Compared to γ phase, there are three inequivalent Li-ion sites (8d, 4c, and 4b) in β phase (Fig. 3a), and the 8d, 4c and 4b sites are 100%, 32%, and 68% occupied, respectively. Thus, Li-ion sublattice is disordered (Li symmetry sites partially occupied) in β-Li_3PS_4. The PS_4 tetrahedron in β phase shows a zig-zag arrangement which provides Li-ion with positions both in octahedral and tetrahedral sites, thereby facilitating interstitial Li-ion diffusion. Liang et al. [19] reported an anomalous high ionic conductivity of nanostructured β-Li_3PS_4 (1.6×10^{-4} S cm^{-1} at 25 °C) (Fig. 3b). Such a nanoporous structure stabilizes preferred β phase and promotes surface conduction. Greenbaum et al. [20] prepared nanoporous β-Li_3PS_4 through thermal decomposition of Li_3PS_4·3THF and found a sulfur-oxygen exchange during the heating process forming PS_3O^{3-} units. They attributed high conductivity to trace amount PS_3O^{3-} units and nanoporous structure. In addition, in the binary Li_2S-P_2S_5 glasses [21], authors suggested that tuning local structure (PS_x-LiS_y polyhedra) could facilitate ionic conduction but $P_2S_7^{4-}$ anion may suppress ionic conduction. Thus, local/microstructure caused by ion-doping in preparation may be another explanation for the high conductivity of nanoporous Li_3PS_4. Now the facilitating role of nanoporous structure in β-Li_3PS_4 calls into question which one, surface conduction or local structure, is the key factor affecting the performance of ionic conduction.

Theoretically, Lepley et al. [22] found that the formation energy of vacancy-interstitial pair in β-Li_3PS_4 was ≤ 0.1 eV, which play a vital role in ion diffusion. Li-ion tends to diffuse along b-axis (8d-4b-8d) due to lower diffusion energy barrier. Xiao et al. [23] studied the doping derivatives of β-Li_3PS_4 (doping at P site and S site) based on the combination of DFT and bond valence methods [24–29]. Oxygen doping reduced Li-ion diffusion activation energy as show in Fig. 3c. Following this work, Xiao et al. [30] further revealed the role of oxygen atoms in β-Li_3PS_4 on ionic conductivity through DFT calculations. They proposed an oxygen-driven transition from two-dimensional (2D) to 3D transport behavior in O-doped β-Li_3PS_4. Yang et al. [31] suggested Li-ion diffusion in the outer of β-Li_3PS_4 nanoporous clusters is much more favorable than in its crystalline forms by AIMD simulation. The diffusion coefficient in nanoporous cluster model was six times higher than that in bulk portion. However, their nanoporous cluster model just has 160 atoms, which may not accurately represent the nanoporous structure. Recently, Shi and Wang et al. [9] studied the elastic properties, defect thermodynamics, electrochemical window, phase stability, and Li-ion mobility of Li_3PS_4. They found the direct-hopping of interstitial Li-ion along the [001] in γ-Li_3PS_4 was energetically more favorable than other diffusion processes, whereas the knock-off diffusion of interstitial Li-ion along the [010] in β-Li_3PS_4 had the lowest diffusion barrier (Fig. 3d).

The $Li_{10}XP_2S_{12}$ (X = Si, Ge, Sn) [32] family is another LISICON-like conductor, and LGPS has the highest ionic conductivity among them

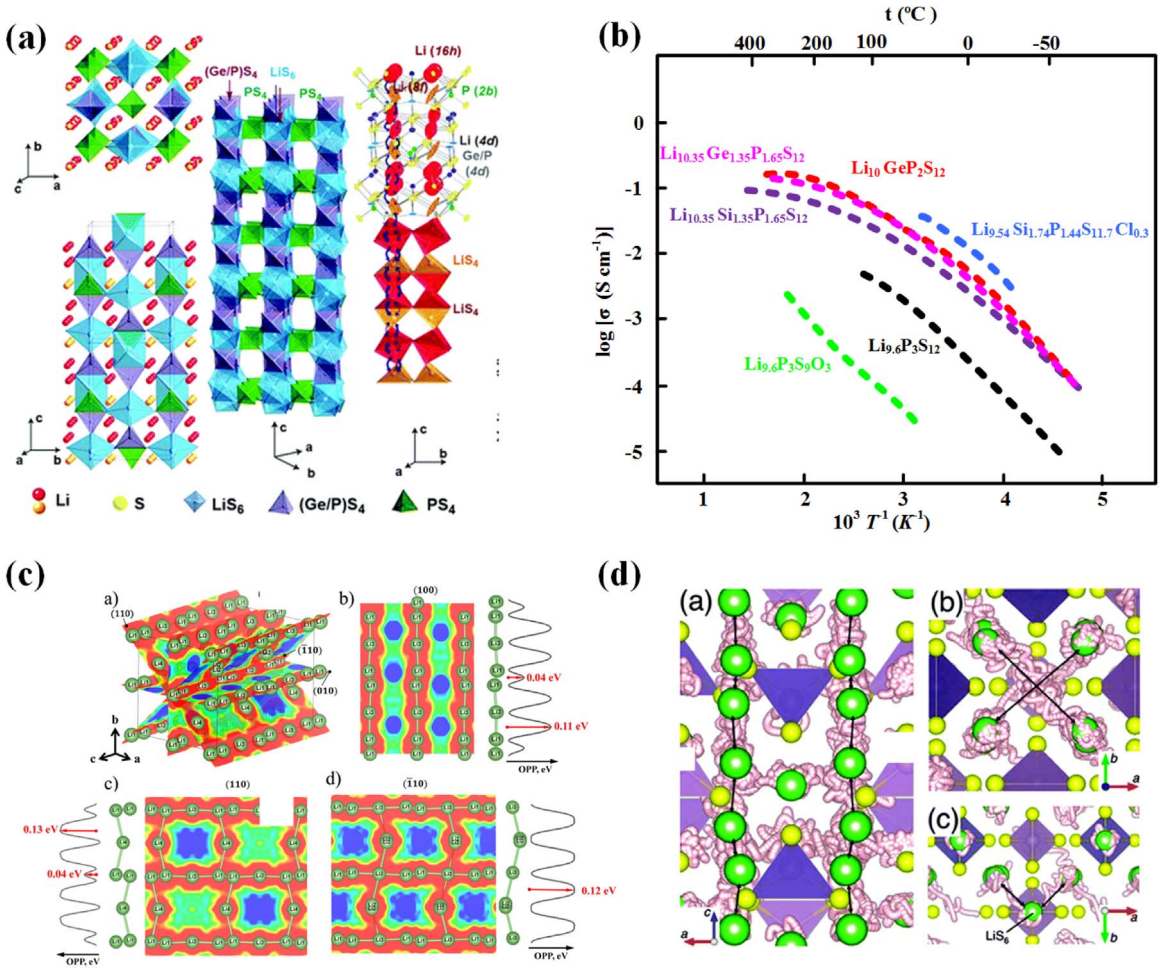

Fig. 4. (a) Crystal structure for LISICON-like conductor $Li_{10}GeP_2S_{12}$ [32]. (b) Reported total ionic conductivity as a functional of temperature for different LISICON-like electrolytes [43]. (c) 3D lithium distribution nuclear density maps for different sections, (100), (010), (110), and ($\bar{1}$10) within the $Li_{10}GeP_2S_{12}$unit cell [33]. (d) Trajectories (white) of Li atoms (Green) for $Li_{10}GeP_2S_{12}$ in ab initio MD simulations at 900 K [35]. PS_4 (GeS_4) tetrahedra in light (dark) purple. S atoms in yellow. (For interpretation of the references to color in this figure legend, the reader is referred to the web version of this article.)

(about 10 mS cm^{-1} at room temperature) (Fig. 4a and b). $Li_{10}GeP_2S_{12}$ (LGPS) has the space group $P4_2/nmc$ which includes $(Ge_{0.5}P_{0.5})S_4$ tetrahedra (4d site), PS_4 tetrahedras (2b site), LiS_6 octahedra (4d), and LiS_4 tetrahedra (8f and 16h sites). In this crystal structure, Li-ions have disordering positions because the occupying rates of 8f and 16h sites are 0.64 and 0.69, respectively. Now, many studies have reported the ion-transport properties of LGPS. Kamaya et al. [32] proposed Li-ions diffuse along one-dimensional (1D) pathway (*c*-direction) formed by LiS_4 tetrahedras. They suggested that 4d octahedral Li atoms were less mobile, so Li-ion diffusion in the *ab* plane was unfavorable. However, Zeier et al. [33] presented NPD data in combination with the analyses of differential bond-valence and nuclear density maps to elucidate diffusion pathways in LGPS. They found LGPS exhibited quasi-isotropic 3D lithium diffusion pathways (Fig. 4c). Liu and Feng et al. [34] approved an anisotropic 3D Li-ion diffusion pathway consisting of an ultrafast 1D diffusion tunnel (activation energy, 0.16 eV) and fast in-plane 2D diffusion (activation energy, 0.26 eV) by multiple solid state NMR methods. Ceder et al. [35] also demonstrated that Li-ion diffusivity in LGPS occurred along 3D rather than 1D pathway using the AIMD method. The diffusion pathway in the *ab* plane connects the 4d octahedral Li-ions to tetrahedral Li (Fig. 4d). Du et al. [36] suggested that there was a strong correlation between Li-ion diffusion barrier and its coordination environment, indicating a very weak anisotropy for Li-ion diffusion of LGPS. Nishino et al. [37] achieved long-time (2-ns) tight-binding molecular dynamics simulations of $Li_{4-x}Ge_{1-x}P_xS_4$ and observed Li-ions diffuse through collective motion. More specifically, Li atom hops to neighbor Li sites through kicking out the Li atom sitting there. Furthermore, excess Li atoms or Li vacancies trigger a new diffusion process where Li atoms are successively kicked out to the Li atoms in (4b) sites, which drastically reduce activation energy. The conclusion is similar to that of Xu et al. [38], who suggested a 1D stringlike cooperative migration mechanism using the AIMD method. Adams et al. [39] studied the structural requirements for Li-ion diffusion in LGPS. They suggested that Li-ion diffusion is dynamically coupled to anion reorientations which drive cation motion via a paddle-wheel mechanism [40] or a temporary opening of percolation pathway [41]. Therefore, the cooperative migration and 3D transport are the most likely explanations to unusually high ionic conductivity of LGPS.

Besides Li-ion diffusion processes, ion-doping, phase stability, and chemical stability for LGPS have also been studied. Ong et al. [42] investigated the $Li_{10\pm1}MP_2X_{12}$ (LMPX, M = Ge, Si, Sn, Al, or P, and X = O, S, Se) family. They found isovalent or aliovalent cation substitutions had small effect on phase/electrochemical stability and Li-ion conductivity but anion substitutions have large effect on these properties. They suggested sulfide LMPX structures were more suitable as Li-ion conductor because the size of S^{2-} is near the size for Li-ion conduction in this structural framework. At high Li chemical potential (μ_{Li}), the LMPX are unstable and tend to form solid electrolyte interphase (SEI) films. At low μ_{Li}, LMPO are easily oxidized and decomposed into $M_xP_yO_z$ and O_2 gas; LMPS and LMPSe are also likely to decompose into P_2S_5 (good glass ionic conductor) and PSe,

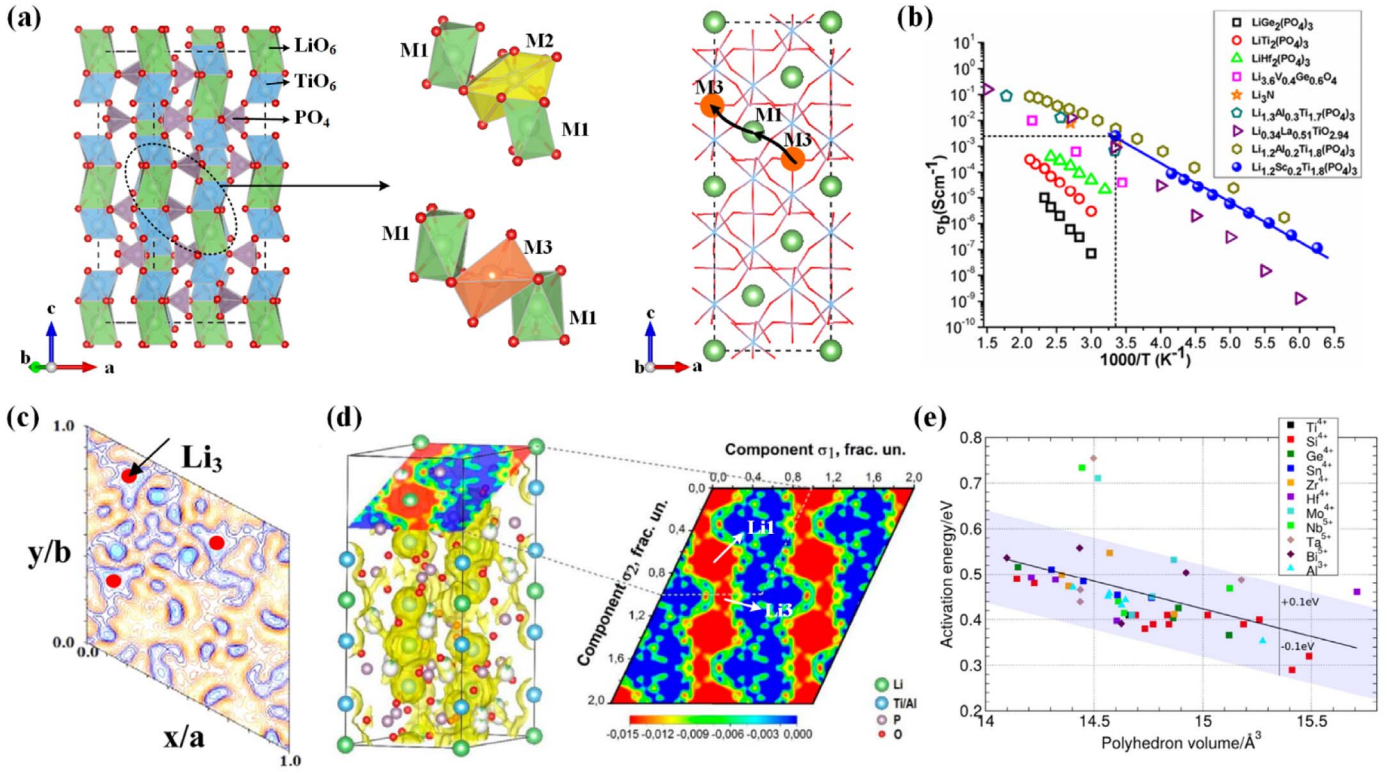

Fig. 5. (a) Crystal structure of $LiTi_2(PO_4)_3$, M1, M2 and M3 sites of Li atoms, and the migration pathway in $LiTi_2(PO_4)_3$. (b) Reported total ionic conductivity as a function of temperature in NASICON type, Li_3N, and perovskite structure [51]. (c) Neutron diffraction patterns of the $Li_{1+x}Ti_{2-x}Al_x(PO_4)_3$ sample recorded at 5 K [52]. (d) Bond valence mismatch in $Li_{1.3}Al_{0.3}Ti_{1.7}(PO_4)_3$ and maximum entropy method reconstructed negative nuclear density maps [56]. (e) Activation energies against the polyhedral volumes of LiO_6 octahedra in the $LiX_{0.2}Ti_{1.8}(PO_4)_3$ [58].

respectively. In addition, cation substitutions have small effect on ionic conductivity but anion substitutions cause different ionic conductivities (the order of conductivity is Se ≈ S > O). However, these results have not been verified by experiments so far. More recently, Kato et al. [43] reported two new ISEs, $Li_{9.54}Si_{1.74}P_{1.44}S_{11.7}Cl_{0.3}$ (LSPSCl) and $Li_{9.6}P_3S_{12}$, which having the same space group with LGPS and showing excellent ionic conductivity, 25 and 10 mS cm^{-1}, respectively. The anisotropic thermal displacement of Li atoms and nuclear density distribution in LSPSCl suggest the 3D Li-ion diffusion pathways. The 2D diffusion in the *ab* plane was induced by the small amount of Cl atoms located in the PX_4 (X = S or Cl) tetrahedral.

2.2.2. NASICON-like

The NASICON framework is originated from the $NaM_2(PO_4)_3$ (M = Ge, Ti, or Zr), generally with a rhombohedral unit cell (space group $R\bar{3}c$), which consists of corner-sharing PO_4 tetrahedra and MO_6 octahedra (Fig. 5a) [44]. Two MO_6 octahedras and three PO_4 tetrahedras share oxygen atoms and create the so-called lantern units, which are assembled to form 3D network structure. When Na atoms are replaced by Li atoms, the material maintains its NASICON structure and turns into Li-ion conductor. There are three different sites in the structure: M1 sites (Li1, 6b, 6-fold oxygen coordination), M2 sites (Li2, 18e, 10-fold oxygen coordination), and M3 sites (Li3, between M1 and M2, 4-fold oxygen coordination). For small tetravalent cations like Ge and Ti, $LiGe_2(PO_4)_3$ (LGP) and $LiTi_2(PO_4)_3$ (LTP) maintain rhombohedral phase, M1 sites are preferentially occupied by Li-ions [45,46]. For larger tetravalent cations like Zr, Sn, and Hf, $LiZr_2(PO_4)_3$, $LiSn_2(PO_4)_3$, and $LiHf_2(PO_4)_3$ are deteriorated to triclinic phase under low temperatures (about under 300 K) and Li-ions are moved to M3 sites [47–49]. All these sites are arranged in alternating way along conducting channels.

Pure LTP has low ionic conductivity at room temperature but isovalent or aliovalent substitution of Ti can enhance its ionic conductivity (Fig. 5b). During recent years, great efforts have been paid to titanium based materials like $Li_{1+x}Ti_{2-x}N_x(PO_4)_3$, $LiTi_{2-x}M_x(PO_4)_3$, and $Li_{1-x}Ti_{2-x}R_x(PO_4)_3$, where N, M, and R stand for tri-, tetra-, and penta-valent cations, respectively. For isovalent substitution, adopting larger M ion size increases the bottleneck size of Li-ion diffusion pathway and thereby, decreases the activation energy of Li-ion diffusion. For aliovalent substitution, the conductivity is increased by increasing mobile lithium concentration and mobility. Especially, Al^{3+} substitution shows large impact on the conductivity of LTP. Bruque and Zahir et al. [50] studied two series of $Li_{1+x}Al_xGe_yTi_{2-x-y}(PO_4)_3$ ($0.2 \le x \le 0.8$; y = 0.8, 1.0) in which larger Ti^{4+} was substituted by smaller Ge^{4+} and Al^{3+} cations. The highest bulk conductivity obtained at room temperature was close to 1.0×10^{-3} S cm^{-1} with low activation energies (≈ 0.35 eV). Arbi et al. [51] studied a series of $Li_{1+x}Ti_{2-x}Sc_x(PO_4)_3$ ($0 \le x \le 0.5$) with XRD, NMR, and IS techniques. They found the $Li_{1.2}Ti_{1.8}Sc_{0.2}(PO_4)_3$ sample exhibited high bulk conductivity (2.5×10^{-3} S cm^{-1}) and low activation energy (0.25 eV) at room temperature (Fig. 6b).

For $Li_{1+x}Al_xTi_{2-x}(PO_4)_3$ (LATP), Arbi et al. [52] indicated that the substitution of Ti^{4+} by Al^{3+} and Li^+ reduced the length of *c* axis but only slightly affected the *a* axis due to the progressive contraction of octahedra (AlO_6) along the *c* axis. Fourier map differences combined with neutron diffraction showed Li-ion occupied preferentially M1 sites in LTP; however, Li ions occupied M1 and M3 sites in LATP (Fig. 5c). The increment of the lithium content favors the occupation of M3 sites, decreasing electrostatic repulsions between Li1 and Li3 ions. The creation of vacancies at M1 sites favors the onset of the fast conduction regime. Redhammer et al. [53] discussed the structure-conductivity relationship of $Li_{1+x}Al_xTi_{2-x}(PO_4)_3$ ($0 \le x \le 0.5$) using a single crystal X-ray and NPD method. They found the additional Li-ions used for charge compensation occupied the M3 sites, which are responsible for the high conductivity of LATP. Arbi et al. [52], Pérez-Estébanez et al. [54], and Redhammer et al. [53] suggested that there were two sites for

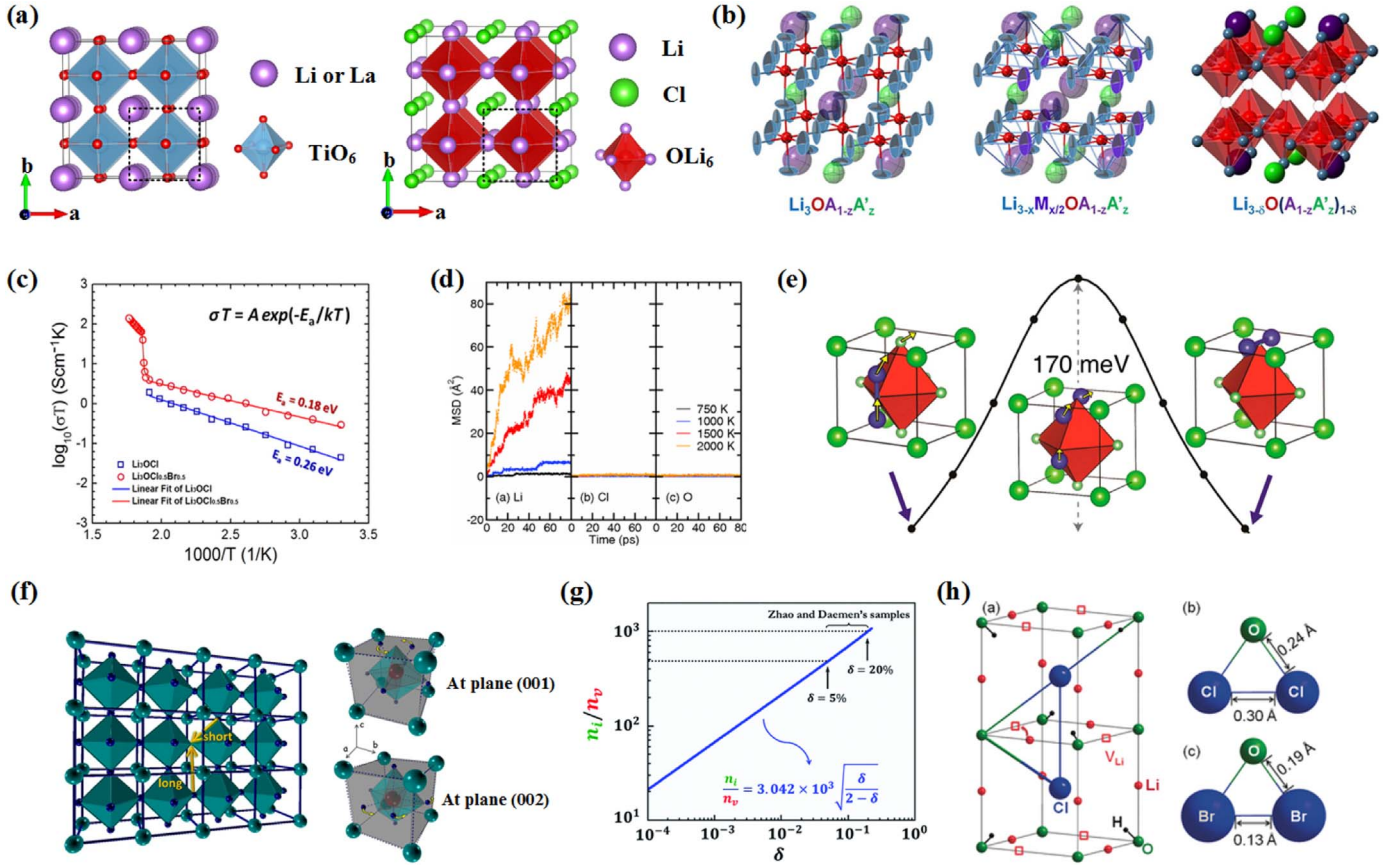

Fig. 6. (a) Crystal structure of perovskite structure $Li_xLa_yTiO_3$ and anti-provskite Li_3OCl. (b) Anti-provskite structure drawing to illustrate the effects of mixing (left), doping (middle), and depletion (right) [101]. (c) Total ionic conductivity for Li_3OCl and $Li_3OCl_{0.5}Br_{0.5}$ anti-perovskites as a function of temperature [101]. (d) Calculated MSD of Li, Cl, and O as a function of time at different temperatures for the disordered 40-atom Li_3OCl supercell with one pair of Cl-O interchanged [100]. (e) Low energy barrier migration pathway in Li_3OCl [103]. (f) Two routes for vacancy migration in Li_3OCl ISE [105]. (g) Ratio between the number of Li interstitials and vacancies in Li_3OCl ISE [106]. (h) Crystal structure of anti-provskite Li_2OHCl [107].

Li-ions in LATP and Li1 content decreased with increased Al substitution. When Ti atoms were completely substituted by Al atoms, that is $Li_3Ti_2(PO_4)_3$, all Li ions were reported to occupy M3/M3′ sites inside M2 cavities [55]. Meanwhile, Senyshyn et al. [56] noted that Li1 content in $Li_{1.3}Al_{0.3}Ti_{1.7}(PO_4)_3$ decreased with increasing temperature, while Li3 content at M3 site increased (Fig. 5d). However, Pérez-Estébanez et al. [54] found the additional Li-ion located at M2′ site (36f, (0.47, 0.31, 0.25)), and the substitution of Al liberated M1 sites, which causing the disorder of Li atoms. This M2′ site is close to M2 sites but displaced in *b* direction from the center of the polyhedron. Therefore, most researchers hold that additional Li-ions used for charge compensation in LATP occupy M3 sites.

Theoretically, Nuspl et al. [57] studied the Li-ion diffusion pathways in LTP and $Li_{1.3}Al_{0.3}Ti_{1.7}(PO_4)_3$ using MD method. From potential energy profile, the energy barrier of Li-ion diffusion in LTP is about 0.30 eV, which is influenced by electrostatic interactions around Li-ion. The Al substitution in LATP only slightly influences energy barrier. Lang et al. [58] studied the ionic conductivity of LTP and related compounds using DFT method. They demonstrated an inverse relationship between activation energy and LiO_6 octahedra size in LXTP (X represents doping cations) (Fig. 5e). But they found the bulk diffusion of LTP was only marginally changed by substitution (activation energies relative to LTP vary within ± 0.1 eV) using vacancy migration, which did not explain the increase in the conductivity of LATP by 3 orders of magnitude than that of LTP. They proposed that the Al substitution increased the Li-ion mobility by increasing Li-ion density and caused interstitial migration with lower activation energy. Now, there are three speculations for the high conductivity of LATP. The first one was the different thermal expansion or anharmonic behavior of oxygen atoms between LTP and LXTP. The second one was low GB conduction derived from the microstructure of LATP. The substitution of Ti^{4+} by Al^{3+} may decrease the energy barrier of GB due to structural change and the degree of densification [59–63]. The last one was Al substitution enhanced the mobility of Li by increasing Li-ion density and lowering activation energies by additional interstitial migration (additional Li3 ions displacing the Li1 sites towards the next Li3 site). In addition, Kang et al. [64] studied the Li-ion conductivity in Al-doped LGP . They suggested that the high ionic conductivity of Al^{3+} doping LGP came from larger Li concentration and new conducting paths with lower activation energy.

However, the first speculation was excluded by Arbi et al. [55], who suggested LTP and LATP had almost the same thermal expansion behavior. For the second speculation, current studies pointed to the opposite conclusion. Aono et al. [65] proposed that Al doping helped to improve compactness and deceased GB resistance, which leading to the high ionic conductivity of $Li_{1.3}Al_{0.3}Ti_{1.7}(PO_4)_3$. Rettenwander et al. [66] measured the ionic conductivity of LTP and LATP single crystals independent of microstructural effects (e.g., grain boundaries, pores, and density) using microcontact impedance spectroscopy. They found the ionic conductivity of LATP (1.73 mS cm^{-1}) was three orders of magnitude higher than that of LTP (3.16×10^{-3} mS cm^{-1}). The LATP and LTP samples had identical densities, where changes in crystal structure were almost linear in the LTP-LATP system by doping Al^{3+} ions. The increase of Li-ion bulk conductivity is intrinsic in nature and the microstructure is excluded as the reason for the high ionic conductivity of LATP. Thus, the speculation needs more studies.

At present, the last speculation is the most likely explanation. Epp et al. [67] revealed several distinct diffusion pathways in

$Li_{1.5}Al_{0.5}Ti_{1.5}(PO_4)_3$ by ^7Li NMR spectroscopy including jumps between two Li sites (M1 and M3). The activation energy of Li-ion diffusion was as low as 0.16 eV deduced from rapid Li exchange, which fully supported recent theoretical work [58]. Recently, Senyshyn et al. [56] studied Li-ion diffusion pathway in $Li_{1.3}Al_{0.3}Ti_{1.7}(PO_4)_3$ by the analysis of neutron and synchrotron-based X-ray powder diffraction data and the MEM. The negative nuclear density maps were reconstructed by the MEM to determine lithium diffusion pathway. They verified a zigzag shape of Li-ion diffusion pathway (M1-M3-M3-M1) with an activation energy of 0.33 eV. Emery et al. [68,69] investigated the $Li_{1.3}Al_{0.3}Ti_{1.7}(PO_4)_3$ by solid-state NMR with local structural and dynamical studies. Li-ion motion occurred through triangular oxygen planes formed between Ti/AlO_6 octahedrons and PO_4 tetrahedrons. This motion induced the Ti/AlO_6 stretching distortion. To date, most bulk activation energies for LATP ranged from 0.15 to 0.33 eV [54,70–72]. Nonetheless, the last speculation was also questioned by Lang et al. [58], who suggested additional Li-ions were easily got trapped near the Al atoms in LATP. Based on the above analyses, we suggest the last speculation is the most likely explanation but the mechanism behind it needs further verification.

Currently, for LATP, the main issue is LATP is not stable in contact with Li-metal. Ti^{4+} in LATP reacts with Li-metal by the form: $Ti_{Ti}^{x} + e \rightarrow Ti_{Ti}^{\prime}$, which leads to electronic conductivity in LATP. Therefore, LATP cannot directly match with Li-metal or low potential anode material. Surface coating of either LATP or anode electrode and an interposed buffer layer are necessary to passivate the interface. Besides LATP, $Li_{1+x}Al_xGe_{2-x}(PO_4)_3$ (LAGP) receives extensive attention and avoids interfacial reduction reaction. Now, the highest reported conductivity of LAGP is about 10 mS cm^{-1} at room temperature [73]. There are many common features between LAGP and LATP such as structure and ion-transport. But GB conductivity of LAGP seems to be higher than that of LATP [74]. TEM results suggest second phases $AlPO_4$ and Li_2O are present at GB following synthesis of LAGP [73,75,76]. $AlPO_4$ and Li_2O could provide alternative diffusion path by the adsorption and desorption of mobile Li-ions at GB and may suppresses the growth of space charge region. For LATP, presence of $AlPO_4$ phase at GB is uncertain. Yamada et al. [77] suggest the phase at GB of LATP is likely to be amorphous LATP-like phase but not $AlPO_4$.

Right now, element-doping, addition of sintering aids [78], surface coating [77] and others are studied for enhancing GB conductivity of LATP or LAGP. The changing of GB conductivity can be explained by three mechanisms. i) The first one is related to the packing of particles and/or the misfit dislocations. The misfit dislocations refers to the lattice mismatch between ISE GBs. The contact among particles becomes more tightly by changing particle sizes and/or morphology. ii) The second one is to form conductive phases or layers at GB, which reduces GB resistance. iii) The last one is change in space charge layer (SCL) or in ion distribution. The SCL effect has been explained by previous studies [79,80]. With the SCL theory, GB conductivity enhancement by coating layer can be explained by the type of charge carrier, $V_{Li}^{\prime}$ for coating layer and $Li_i^{\bullet}$ (interstitial Li) for ISE. Coating layer adorbs mobile Li-ion at the surface meaning Li depletion for ISE and Li accumulation for coating layer, which leads to low interfacial resistance.

2.2.3. Perovskite and anti-perovskite

2.2.3.1. Perovskite. Among oxide-based ISEs, perovskite-type structure ABX_3 (A = Ca, Sr or La; B = Al or Ti; X = O) received great interest because of their potential applications in ASSLBs. The ideal perovskite structure with cubic unit cell and space group $Pm\bar{3}m$ consists of A-ions at the corner, B-ions at the center, and oxygen at the face-center. A-ions are in 12-fold coordination and B-ions are in 6-fold coordination (BX_6) that share corners with each other (Fig. 6a). The introduction of lithium in ABX_3 changes the concentrations of both lithium and vacancies. The vacancies concentration and their interactions lead to the ordering of lithium/vacancies in the planes perpendicular to the *c*-axis, which significantly affects ionic conductivity. Li-ions diffuse in the *ab* plane by vacancies. The diffusion bottleneck is a square-planar made of oxygen [81]. The bottleneck size can be increased by placing large rare-earth or alkaline-earth metal ions in the A site. The larger the bottleneck, the higher the ionic conductivity [82].

Among perovskite-type solid electrolyte materials, LLTO exhibited very high bulk ionic conductivity above 10^{-3} S cm^{-1} at room temperature [83–87]. LLTO displays an alternate stacking with La-rich/La-poor layers in the crystal structure. Li-ions tend to diffuse within the La-poor layers as that forms a percolation pathway for Li-ion migration. However, the large GB resistance results in a total conductivity of only 10^{-5} S cm^{-1} at room temperature [88]. Now, the microscopic mechanism responsible for this GB resistance has not been totally elucidated [89]. Chi et al. [90] studied the origin of the large GB resistance in LLTO through atomic-resolution STEM/EELS analysis. The results suggested that both Li and La at grain boundaries were locally depleted, TiO_6 octahedral undergone significant deformation, and partial Ti^{4+} were reduced to Ti^{3+}. The GB structure is not energetically preferred for either Li accommodation or transport. But the STEM just revealed the misfit dislocations in LLZO and they didn't detect the SCL which is part of GB. The SCL may be another explanation for the large GB resistance. Moreover, Ti^{4+} is easily reduced to Ti^{3+} when contacting with Li-metal anode [88,91]. LLTO phase constituent is difficult to be controlled because high temperature causes Li_2O loss during synthesis [83]. These factors limit the application of LLTO in ASSLBs.

2.2.3.2. Anti-perovskite. In LLTO, Li-ion is at the A sites. But for F-ion conductor, $NaMgF_3$ and $KMgF_3$, F-ion is the carrier and is at the X sites [92–95]. Perovskite-type fast ion conductors are generally used as electrodes and ISEs in fuel cells with O^{2-} ion at X sites [96]. Inspired by these materials, Zhao et al. [82] proposed a novel family of lithium-rich anti-perovskite (LiRAP) Li_3OX (X = Cl or Br) as fast Li-ion conductors (Fig. 6a). They found the structure of LiRAP could be manipulated quite easily by substitution, e.g., introducing large Br anions at dodecahedral site to replace Cl anions. Fig. 6b illustrates three methods to manipulate the structure of anti-perovskite: mixing (left), doping (middle), and depletion (right). The substitution makes the following two effects on structures: (i) tuning vacant concentration and ionic hopping via the Schottky route; (ii) tuning lattice volume and bottleneck size for Li-ion diffusion. In Fig. 6b (left and middle), flattened thermal ellipsoid indicates a shallow and flat energy well, which enhances the mobility of Li-ion. They speculated that the soft phonon-driven structural phase transitions in the anti-perovskites could actively promote Li-ion transport. Fig. 6c shows the Arrhenius plots for the ionic conductivities of Li_3OCl and $Li_3OCl_{0.5}Br_{0.5}$. They found there was a phase transition for both materials when the temperature above 247 °C and the ionic conductivity of $Li_3OCl_{0.5}Br_{0.5}$ sharply increased (6.05×10^{-3} S cm^{-1}). However, their ionic conductivities at room temperature were low. Li-ions bond tightly at octahedral vertices and coordinated with two oxygen anions as the nearest neighbors. The stable Li_6O structure provided no ionic hopping mechanism and resulted in low conductivity. They suggested ionic conduction is related with the LiCl deficiency which introduced empty dodecahedral Cl-sites and Li vacancies at the octahedral vertex. Recently, Zhu et al. [97] demonstrated that mixing $Li_7O_2Br_3$ into Li_3OBr could enhance the conductivity of Li_3OBr. The ionic conductivity of $Li_7O_2Br_3$:Li_3OBr composite mixture with weight percentage ratio of 44:56 was 2.4×10^{-5} S cm^{-1} at room temperature, which is more than one order of magnitude higher than that of pure-phase Li_3OBr. $Li_7O_2Br_3$ is layered anti-perovskite structure and a secondary phase during the Li_3OBr synthesis. However, they did not

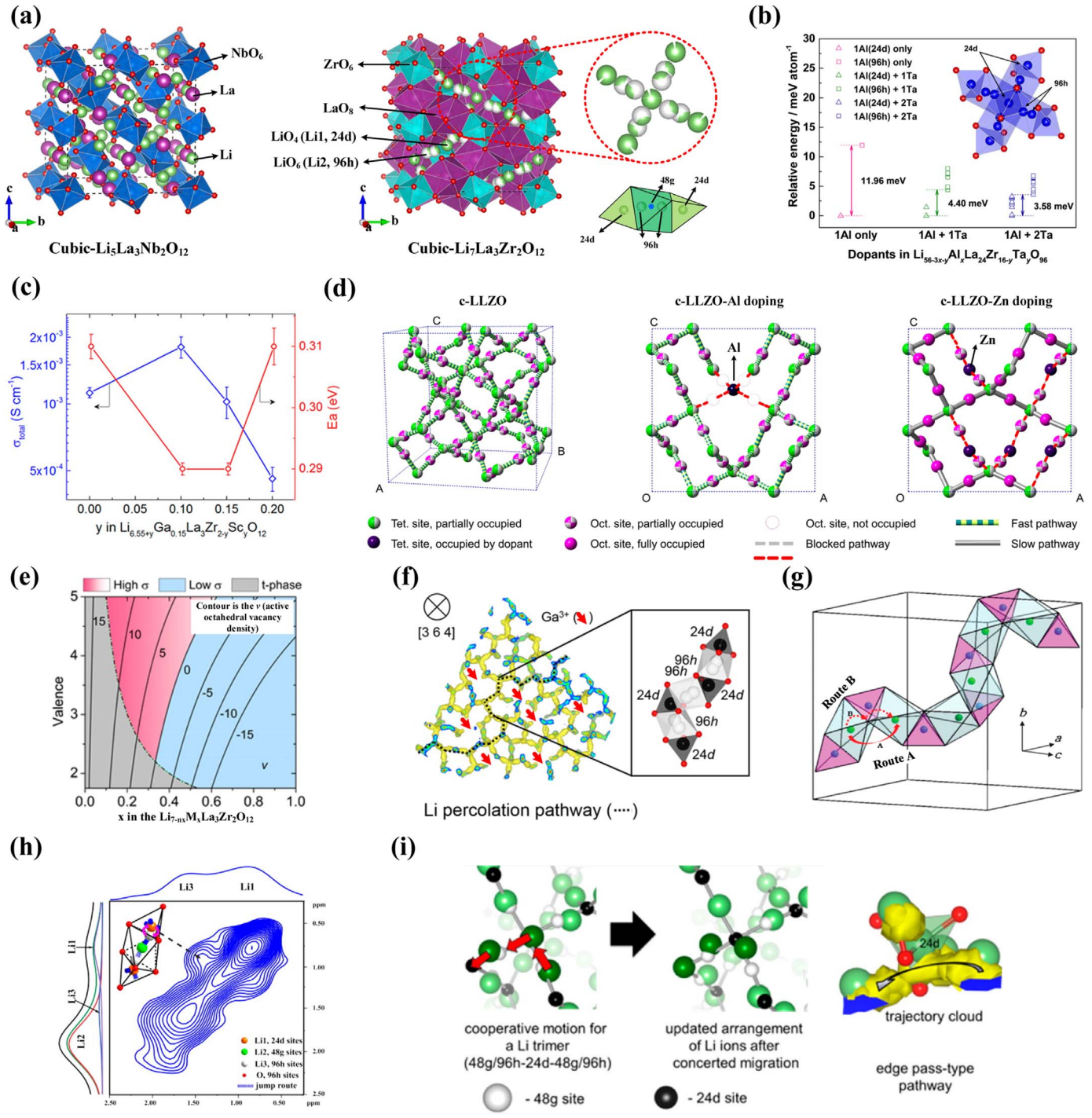

Fig. 7. (a) Structure of garnet-type c-LLZO, and three Li-ion sites. (b) The calculated energies of LLZO with Al in 24d and 96h site. Ta doping effect on change of Al site preference in Al-doped LLZO [126]. (c) Total ionic conductivity and activation energy at various doping levels in $Li_{6.55+y}Ga_{0.15}La_3Zr_{2-y}Sc_yO_{12}$ [120]. (d) 3D Li-ion migration pathway in c-LLZO, c-LLZO-Al doping, and c-LLZO-Zn doping systems [123]. (e) Relationship between the active octahedral vacancy density (υ) in a unit cell and the valence n and doping level x in the $Li_{7-nx}M_xLa_3Zr_2O_{12}$ [123]. (f) Li trajectory density in in $Li_{7-3x}Ga_xLa_3Zr_2O_{12}$ [136]. Red arrows and the dashed line indicate lost Li paths and percolated Li pathway (retained), respectively. (g) Connectivity of LiO_6 and LiO_4 polyhedra in garnet ISEs including route A and route B [137]. (h) ^{6}Li-^{6}Li exchange spectra of $Li_{7-2x-3y}Al_yLa_3Zr_{2-x}W_xO_{12}$ (x = 0.5) [139]. (i) Network and diffusion pathway of Li sites in cubic $Li_7La_3Zr_2O_{12}$ using MD simulation method [145]. (For interpretation of the references to color in this figure legend, the reader is referred to the web version of this article.)

yet obtain a pure phase of $Li_7O_2Br_3$. Interestingly, compared with other fast ion conductors with perovskite structure such as Ag_3SI [98,99], Li_3OX has highly ordered O- and X-ions but anions (S and I) are disordered in Ag_3SI.

Theoretically, Zhang et al. [100] simulated Li-ion diffusion in Li_3OX using AIMD method. They found the occurrence of Li-ion diffusion was accompanied by an order-disorder transition of Li-ion sublattice. The melting temperature of Li-ion sublattice was below that of its crystal structure (Fig. 6d), which agreed with experimental observation [101]. In the perfect crystal structure, the MSD of Li-ion began to increase drastically at 2000 K. Meanwhile, the MSD of anions (O and Cl) also increased with time, indicating a melting of entire crystal structure. When vacancy or anion disorder was introduced into the Li_3OX, the

melting temperature of Li-ion sublattice was greatly reduced, and Li-ion sublattice melting preceded the melting of anions. Therefore, the mobile Li vacancy and anion disorder were main driving forces for ionic conductivity in Li_3OX. They evaluated different vacancy types and calculated hopping between vacancy and Li-ion in Li_3OCl. However, all calculated activation energies (0.367–1.201 eV) were higher than experimental value (0.26 eV) [101]. For $Li_3OCl_{0.5}Br_{0.5}$, the calculated activation energy (0.288–0.332 eV) via vacancy migration was also higher than that of experiment (0.18 eV) [101]. The presence of halogen vacancies (LiX-deficient sample, X = Cl or Br) did not benefit the Li-ion diffusion in Li_3OX, which was contrary to experimental suggestion that LiX-depletion enhanced Li-ion hopping [101]. Deng et al. [102] further identified a lower barrier of Li vacancy (282 meV) in Li_3OX by varying the halide sublattice ordering. They suggested that a Cl-rich channel with Br-rich endpoints configuration led to low vacancy migration barriers in Li_3OX structure. The AIMD simulations suggested that $Li_3OCl_{0.75}Br_{0.25}$ had a higher Li-ion conductivity than $Li_3OCl_{0.5}Br_{0.5}$.

Emly et al. [103] proposed interstitial migration mechanism with a dumbbell structure (Fig. 6e). The activation energy for interstitial migration was 0.17 eV in Li_3OCl lower than that of experiment (0.26 eV) [101]. But the formation energy of Frenkel defect (interstitial Li-ion) within a 6 × 6 × 6 supercell was up to 1.94 eV. In another explanation by Lu et al. [104], they considered three types of defects: LiCl Schottky, Li_2O Schottky, and Li interstitial with a substitutional defect of O on a Cl site ($Li_2O + Cl_{Cl}^{X} \rightarrow Li_i^{\bullet} + O_{Cl}^{'} + LiCl$). The LiCl Schottky is equivalent to LiCl-deficient in previous theoretical work [105]. They found the formation of LiCl-deficient was the most energetically favorable and LiCl-deficient was the best for Li-ion migration with low activation energy. In $Li_{3-x}OCl_{1-x}$ ($0.01 \le x \le 0.15$) crystal with LiCl-deficient, Li-ions migration went through the pathway between $V_{Cl}^{'}$ pairs, and activation energies (ranging from 0.347 eV to 0.312 eV) decreased with increasing LiCl-deficient concentrations. Thus, they proposed that Li vacancy hopping is the main diffusion mechanism in Li_3OCl. Mouta et al. [105] further determined the diffusion mechanism in Li_3OCl employing classical atomistic quasi-static calculations (Fig. 6f). The formation energy of LiCl-deficient was 0.93 eV at 0 K and 1.01 eV at 300–500 K. The formation energy of Frenkel defects was 1.59 eV at 0 K and 1.62 eV at 300–550 K, which was lower than the value of 1.94 eV reported by Emly et al. [103]. In stoichiometric crystal, vacancy concentration was several orders higher than that of interstitial concentration, suggesting Li vacancies were the charge carriers of Li_3OCl. However, in the LiCl-deficient crystal, charge compensating mechanisms could increase the concentration of interstitials, and the ionic conduction was likely to be driven by interstitial migration. In the following work, Mouta et al. [106] considered two possible LiCl-depletion Li_3OCl configurations and demonstrated that Li-ion interstitials outnumber vacancies by 2–3 orders of magnitude in LiCl-deficient Li_3OCl using the same method based on interionic potentials (Fig. 6g). Thus, in LiX-deficient Li_3OX crystal, interstitial mechanism is responsible for ionic conduction.

Based on the above analyses, we think that the Li-ion transport mechanism in Li_3OX remains inconclusive. For vacancy mechanism, the activation energy of theoretical studies [100,105] is higher than the experimental value [101]. For interstitial mechanism, the activation energy of theoretical studies [103] is lower than the experimental value [101]. But the formation energy of interstitial is higher than that of vacancy [105]. A further understanding of the defect chemistry and ion-transport pathway is necessary by using theoretical methods.

In addition to Li_3OX, Li_2OHX also has anti-perovskite structure (Fig. 7h) [107,108]. In the cubic Li_2OHX, H-ions tend to form linear O-H-Cl bonds in Li_2OHCl and Li-ions form linear O–Li–O bonds. Ordered Li vacancies make each O-ion coordinated by 4 Li^+ and 2 H^+ cations. Li-ions migrate via Li vacancy through a triangular $O^{2-}(Cl)^{-}_2$ site (Fig. 6h). Thus, the Li-ion migration is hindered by the coulomb repulsion and steric hindrance of the H^+ ions with a fixed O-H-Cl hydrogen bond. Liang et al. [109] found overcooling process could tuning the concentration of defects, and thus affect the ionic conductivity of Li_2OHCl. Li et al. [108] found the ionic conductivity of $Li_2(OH)_{0.9}F_{0.1}Cl$ (part of OH-ions replaced by F-ions) was close to Li_2OHCl reported by Liang [109], but was about 2 orders of magnitude lower than Li_3OCl reported by Zhao [101]. Therefore, further studies should be done to enhance the ionic conductivity of Li_2OHCl.

2.2.4. Garnet

Ideal garnets process a general chemical formula of $A_3B_2(XO_4)_3$ (A = Ca, Mg, Y, La or rare earth; B = Al, Fe, Ga, Ge, Mn, Ni or V; X = Si, Ge, Al) where A, B and X are 8-, 6- and 4-fold coordinated cation sites, which crystallize in a face centered cubic structure with the space group *Ia*-3*d*. In garnet-type ISEs, $Li_3Ln_3M_2O_{12}$ (Ln = lanthanides; M = Te, W), $Li_5La_3M_2O_{12}$ (M = Nb, Ta, Sb), $Li_6ALa_2M_2O_{12}$ (A = Ca, Sr, Ba, Mg; M = Zr, Sn, Ta, Nb), and $Li_7La_3M_2O_{12}$ (M = Zr, Sn) were widely studied. Among them, $Li_5La_3M_2O_{12}$ was the first reported Li-stuffed garnet. Fig. 7a shows the ideal crystal structure of $Li_5La_3M_2O_{12}$. For $Li_5La_3M_2O_{12}$ (M = Nb, Ta), La and M sites can be substituted by other metal ions leading to Li-rich garnet, such as $Li_6(Ala)_3Zr_{1.4}Ta_{0.6}O_{12}$ (A = Mg, Ca, Sr, Ba), $Li_{6.4}La_3XO_{12}$ (X = $Zr_{1.4}Ta_{0.6}$, $Zr_{1.7}W_{0.3}$), and $Li_7La_3Y_2O_{12}$ (X = Zr, Sn). In $Li_5La_3M_2O_{12}$, Li-ions are distributed at both tetrahedral (24d) and distorted octahedral (48g/96h) sites, which was confirmed by Cussen et al. [110–112] using NPD method. For $Li_7La_3Zr_2O_{12}$, there are two phases: high-temperature cubic phase (space group *Ia*-3*d*) and low-temperature tetragonal phase (space group *I*41/*acd*). The cubic-LLZO (c-LLZO) exhibited higher ionic conductivity than tetragonal-LLZO (t-LLZO). In c-LLZO, there are three occupied sites for Li-ions, tetrahedral sites (24d), octahedral sites (48g), and off-centered octahedral sites (96h), respectively. Li-ion sublattice is always ordered (all Li sites either full or empty) in t-LLZO, while the Li sublattice is always disordered (all Li symmetry sites partially occupied) in c-LLZO. The 3D network structure in c-LLZO is formed by face-shared tetrahedral and octahedral.

Partial or total substitution at La and/or M sites for garnet-type ISEs is an important strategy to tune their ionic conductivity. Among doping compounds based on $Li_5La_3M_2O_{12}$, Ta-doped garnet, $Li_{6.4}La_3Zr_{1.4}Ta_{0.6}O_{12}$ (LLZTO), had an ionic conductivity 1.0 mS cm^{-1} at room temperature with apparent activation energy of 0.35 eV [113]. Later, Wang et al. [114] prepared dense LLZTO sheets and obtained a conductivity of 1.02 mS cm^{-1} at room temperature. Thangadurai et al. [115] studied the $Li_{6.65}La_{2.75}Ba_{0.25}Zr_{1.4}Ta_{0.5}Nb_{0.1}O_{12}$ and $Li_{6.4}La_3Zr_{1.4}Ta_{0.6-x}Nb_xO_{12}$ (x = 0, 0.1, 0.2, and 0.3) by La-Zr double-doping (La-sites substitution with Ba and Zr-sites substitution with Ta and Nb). They found the $Li_{6.4}La_3Zr_{1.4}Ta_{0.6}O_{12}$ member exhibited high bulk ionic conductivity of ~ 0.7 mS cm^{-1} at room temperature with an activation energy of 0.26 eV. For c-LLZO, Inada et al. [116] synthesized $Li_{6.5}La_{3-x}Ba_xZr_{1.5-x}Ta_{0.5+x}O_{12}$ (LLBZT) ISE by adopting La-Zr double-doping means (La-sites substitution with Ba and Zr-sites substitution with Ta). Their results suggested that the optimum doping proportion on the ionic conductivity of LLBZT were 0.1 Ba and 0.6 Ta, respectively. The activation energies of Li-ion diffusion decreased with the increasing of Ba content. Bernuy-Lopez et al. [117] studied the Ga-substituted $Li_7La_3Zr_2O_{12}$ and found the substitution of Li by Ga created Li vacancies which enhancing the Li-ion conductivity. Guo et al. [118] also studied the Ga-doped LLZO and gave the optimum Ga concentration in $Li_{7-3x}Ga_xLa_3Zr_2O_{12}$. Rettenwander et al. [119] prepared the Ga and Al co-doped samples $Li_{6.4}Al_{0.2-x}Ga_xLa_3Zr_2O_{12}$, and ionic conductivity increased from 2.6×10^{-4} to 1.2×10^{-3} S cm^{-1} at room temperature. Buannic et al. [120] presented La-Zr double-doping (La-sites substitution with Ga and Zr-sites substitution with Sc) to improve ionic conductivity of c-LLZO. They suggested that double-doping resulted in a unique Li-ion local structures enhancing ionic conductivity and lowering activation energy.

The ion substitution is also helpful to stabilize high conductive cubic phase and suppress the formation of low conductivity phases,

especially Al-dopant. However, for Al-doped c-LLZO, there are some debates. The first disputed point is the site of Al-dopant in c-LLZO. Geiger et al. [121] found there are two different Al positions (24d and 96h sites) in c-LLZO by ^{27}Al NMR spectra. Yang et al. [122] and Buschmann et al. [112] also employed ^{27}Al NMR method to elucidate the occupied sites of Al. They suggested that Al-ions were located on the 24d sites. NPD studies also had opposite results, most studies suggested Al-ions were located at the 24d sites [119,123,124]; few suggested Al-ions were at the 48g sites [124]. Theoretically, Rettenwander et al. [125] indicated that Al-ions at 24d sites are energetically favorable, followed by Al-ions at 96h and 48g. Shin et al. [126] gave the same results but the Ta-ions incorporation ($Li_{7-3x-y}Al_xLa_3Zr_{2-y}Ta_yO_{12}$) could displaced most of Al-ions from the 24d to 96h sites, providing more open space for Li-ion transport as well as the increased amount of Li vacancy. The calculated energies of LLZO with Al in 24d and 96h sites are shown in Fig. 9b.

The second argument point is the role of Al-dopant in stabilizing c-LLZO. Although almost all studies agree that Al-dopants at 24d sites block the Li-ion diffusion path [123,126,127], how Al-dopants stabilized the cubic phase of LLZO and whether Al-dopants could reduce ionic conduction are still contentious questions. Buschmann et al. [110–112] suggested the Al-doping could stabilize the c-LLZO phase by enhancing the disordering of Li-ion sublattice. Each Al-ion replaced three Li-ions at the 24d site for charge neutrality, and thus each Al-ion made two Li vacancies. Adams et al. [128] found that structural phase transition temperature (t-LLZO → c-LLZO) was low at $Li_{6.5}$ content, and the substitution of Ta^{5+} on Zr^{4+} increased Li vacancy concentration to stabilize the cubic structure. Bernstein et al. [129] suggested Li-ion vacancies increased configurational entropy of LLZO and reduced energy gain from disordering, which leading to a low phase transition temperature. Therefore, the vacancies in Li sublattice introduced by ion-doping stabilized the cubic phase. An et al. [130] studied the synthesis of Al-doped LLZO by in-situ NPD method to visualizing the structure's evolution in real time. In Al-free LLZO sample, the evaporation of Li_2CO_3 in the synthesis process of LLZO caused the low conductivity intermediate phases ($La_2Zr_2O_7$ and Li_2ZrO_3). They found Al-dopant promoted the completion of formation reaction for c-LLZO. However, Al-dopant also led to a side reaction to low conductivity phases such as $LaAlO_3$ and $LiAlO_2$. Ying et al. [131] found that Al-doping content is vital for the stability of c-LLZO. When Al-doping content was low (0.2 and 0.7 wt%), LLZO exhibited both phases (c-LLZO and t-LLZO). When Al-doping content reached the 1.2 wt%, only c-LLZO was present. When Al-doping content was high (2.5 wt%), the La_3AlO_3 impurity would exit in the sample. But the EIS results indicated that La_3AlO_3 had little effect on ionic conductivity.

It is generally agreed that the effects of ion substitution on ionic conductivity as well as migration pathway are due to the change of the Li-ions content and the Li-ions distribution over tetrahedral and octahedral sites. For alkaline earth ions doped $Li_{5+x}A_xLa_{3-x}Ta_2O_{11.5+0.5x}$, Murugan et al. [132] found the ionic conductivity was controlled by both lithium and oxygen concentration. In the following work, they pointed out that the ionic conductivities of $Li_6BaLa_2Ta_2O_{12}$ and $Li_5La_3Ta_2O_{12}$ were dependent on the concentration and mobility of mobile Li-ions [133]. Ba substitution had an order of magnitude increase in the concentrations of mobile Li-ion. The concentration of mobile Li-ion was independent on temperature. The mobility of Li-ion was related to the occupancy of Li-ion in the tetrahedral sites of garnet phases. Cussen et al. [134] studied the $Li_{5+x}Ba_xLa_{3-x}Ta_2O_{12}$ (LBLTO) using NPD method. They found Li-ions at the central 48g sites moved towards the off-centered 96h sites within the octahedral sites due to repulsive forces between Li-ions in tetrahedral sites and octahedral sites. In the following work [135], they found the occupancy of distorted octahedral sites in $Li_{3+x}Nd_3Te_{2-x}Sb_xO_{12}$ increased with lithium content, while the occupancy of tetrahedral sites reduced. The fast ionic conductivity occurred via a network of edge-linked distorted oxide octahedral with tetrahedral sites playing no part in diffusion properties. Buannic et al. [120] found high Sc substitution content of $Li_{6.55+y}Ga_{0.15}La_3Zr_{2-y}Sc_yO_{12}$ resulted in low ionic conductivity, as shown in 9c. To find out, they investigated the occupation of Ga and Li in $Li_{6.55+y}Ga_{0.15}La_3Zr_{2-y}Sc_yO_{12}$ (LGLZSO) with low (y = 0.10) and high (y = 0.20) Sc content using NMR and DFT methods. Under low Sc content, Ga was at 24d sites for low Sc content, and the presence of Sc increased both the concentration and disorder of the Li in LGLZSO. Under high Sc content, Ga moved from tetrahedral 24d to octahedral 96h sites, hindering the Li percolation network. Based on these analyses, they suggested that the Li-ion mobility at 96h sites was higher than 24d sites. This is consistent with what Shin et al. [126] suggested in the double-doped $Li_{7-3x-y}Al_xLa_3Zr_{2-y}Ta_yO_{12}$. An et al. [123] studied $Li_{6.28}Al_{0.24}La_3Zr_2O_{12}$ and $Li_{5.8}Zn_{0.6}La_3Zr_2O_{12}$ using in-situ NPD experiments. They suggested that ionic conductivity was determined by active vacancy density, meaning the density of octahedral site vacancy (Fig. 7d and e). The active vacancy density could be controlled by the valence and concentration of aliovalent doping. High ionic conductivity of LLZO could be obtained by high valence dopants. The high valence dopants could not only suppress the formation of low conductivity phases such as secondary phases and tetragonal phase, but also increased the content of active vacancy. Jalem et al. [136] found Ga-dopant did not change the lattice constant nor contribute to any significant structural distortion using MD simulation. They found a decreasing trend under low Ga content and flat trend under high Ga content. The density plots of mobile Li-ions suggested Li-ion transport pathways were interrupted by Ga, as shown in Fig. 7f.

Li-ion transport mechanism in garnet-type conductors was studied by experimental and theoretical methods. Cussen et al. [134] observed Li···Li dimers with short distance of 2.44 Å in LBLTO by NPD method. The high displacement parameters of Li-ions at 24d sites and the short distances suggested a complex cooperative mechanism in LBLTO. For migration pathway, two potential pathways are proposed by Baral et al. [137], as shown in Fig. 7g. In route A, Li-ions migrate between two octahedral Li sites via interstice bypassing their common tetrahedral neighbor, i.e., the tetrahedral Li sites do not participate in the migration process. In route B, Li-ions move through shared triangular faces that separate the octahedral and tetrahedral polyhedral, i.e., Li-ions at tetrahedral sites participate in the migration process. The route A was suggested by Li NMR studies by Cussen et al. [135] and Wullen et al. [138]. Cussen et al. did not find the Li-ion movement or hopping between tetrahedral and octahedral sites in $Li_{3+x}Nd_3Te_{2-x}Sb_xO_{12}$. Wullen et al. found both ^{6}Li-[55]-CPMAS-NMR spectra and 2D exchange NMR in $Li_5La_3Nb_2O_{12}$ suggested that Li-ion migration from one octahedral site to another, whereas the tetrahedral sites seemed to act as a trap for Li-ions. However, the route B was also evidenced by NMR. Using high resolution NMR in a series of $Li_{7-2x-3y}Al_yLa_3Zr_{2-x}W_xO_{12}$, Wang et al. [139] demonstrated a Li-ion migration path of 24d-96h-48g-96h-24d and found Li-ion migration at 24d sites is the rate-determining step (Fig. 7h). The results were consistent with another experimental observation using high temperature NPD techniques coupled with MEM analysis [53,113,122,140–143]. They also found a Li-ion 3D diffusion pathway consisting of interlocking Li(24d)-Li(96h)-Li(48g)-Li(96h)-Li(24d) chain segments. Using DFT calculations, Xu et al. [144] found that Li-ion migration through tetrahedral sites had lower energy barrier, suggesting tetrahedral sites participated in the diffusion process. Jalem et al. [145] investigated ion-transport mechanism in c-LLZO using AIMD calculations. They suggested high bulk conductivity was attributed to the cooperative diffusion of Li-ions at adjacent tetrahedral and octahedral sites, in which the cooperative diffusion occurs under two conditions: (i) Li arrangement with the 48g/96h-24d-48g/96d, (ii) unstable residence of Li-ion at the 24d sites (Fig. 8i). Jalem et al. [146] further studied Li-ion dynamics in garnet cubic $Li_5La_3Ta_2O_{12}$ by AIMD calculations. They found the Li-ion transport follows a cooperative mechanism with the presence of vacancy dimers. Now, it appears that route B is more persuasive than route A.

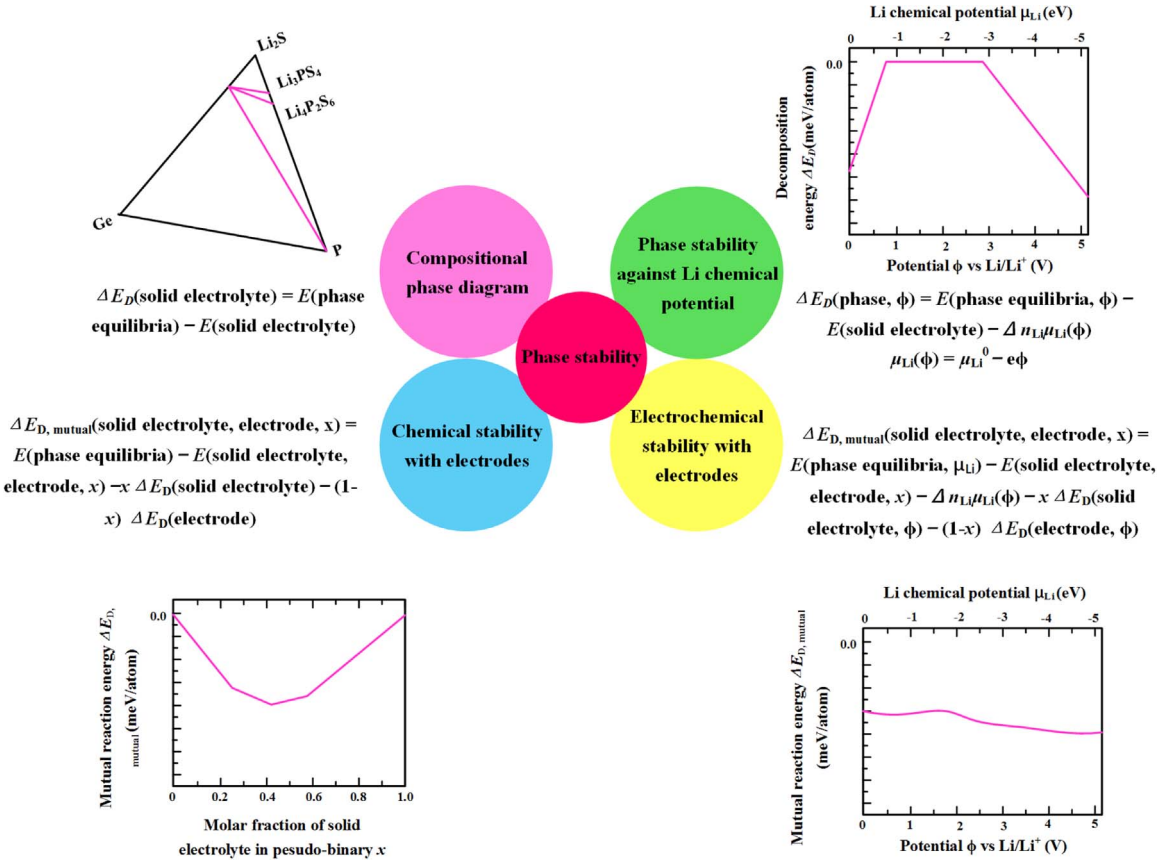

Fig. 8. Schematic representation of different phase stability.

Based on the above analyses, recently more and more researchers tend to the route B, that is, Li-ion migration occurs through tetrahedral sites. However, as mentioned in the prior paragraph, recent studies by Buannic et al. [120] and An et al. [123] implied Li-ion mobility at octahedral sites was higher than tetrahedral sites. Therefore, we believe further study is necessary to fully understand the mechanism of Li-ion transport in garnet ISEs.

3. Stability: phase stability and interfacial stability

3.1. Phase stability

Phase stability is an essential problem for ISEs. Deep understanding on phase stability is helpful to obtain target products with optimized structures and compositions and to offer the information of safe and stable working conditions. Phase composition and phase evolution can be illustrated concisely and directly in the phase diagram. Here, we briefly summarize typical research activities on phase diagram and phase stability for ISEs (Fig. 8). Pseudo-binary phase diagram is a useful tool to study the phase transition of electrolytes with temperature and composition. Compositional phase diagram can evaluate the phase equilibria of ISEs with composition. Grand potential phase diagram can evaluate the stability of a specific ISE in equilibrium with an external environment. Usually, the phase equilibria of ISEs are in equilibrium with an opening lithium sink of μ_{Li}. By studying phase equilibria and decomposition reaction energies of ISEs with respect to μ_{Li}, we can evaluate the chemical/electrochemical stability and the decomposition interphases of ISEs, and thus quantify the extension of electrochemical window.

The chemical and electrochemical stabilities of ISEs have been studied in detail by theoretical calculations [35,147–151]. Mo et al. [35] studied lithium grand potential phase diagrams of the Li-Ge-P-S system at various μ_{Li}. They suggested that LGPS got reduced by lithium insertion at high μ_{Li}, resulting in LGPS decomposition (Li_2S, Li_3P, and $Li_{15}Ge_4$). With the decrease of μ_{Li}, LGPS got oxidized by lithium extraction and was decomposed into LiXS system (Li_3PS_4 and Li_4GeS_4) and XS system (P_2S_5, S, and GeS_2). Thus, LGPS is instable against Li-metal or high voltage cathodes materials. Shi and Wang et al. [9] used similar approach to construct the lithium grand potential phase diagrams of the Li-P-S system to examine the phase equilibria of Li_3PS_4. According to their results, the intrinsic stable range of Li_3PS_4 was limited to 1.72–2.31 V (corresponding to -3.62 to -4.21 eV of μ_{Li}). Richards et al. [152] studied the pseudo-binary phase diagram of the $LiZnPS_4$-γ-Li_3PS_4 system by the combination of phonon and cluster expansion with MC calculations. The phase diagram showed that the $Li_2Zn_{0.5}PS_4$ composition was stabilized above 950 K.

For anti-perovskite type Li_3OX, Emly et al. [103] found the anti-perovskite Li_3OX was metastable to be relative to Li_2O and LiX. Although the band gap of Li_3OCl exceeded 5 eV, Li_3OCl was decomposed into Li_2O_2, LiCl, and $LiClO_4$ above 2.5 V, suggesting that these anti-perovskite materials were only suited for low-voltage Li batteries. Zhang et al. [100] constructed the ternary Li-O-Cl and Li-O-Br phase diagrams using well-known Li-O-Cl and Li-O-Br compounds. They suggested that Li_3OX was energetically unstable at 0 K and the reaction, Li_3OCl (Li_3OBr) → Li_2O + LiCl (LiBr), would happen spontaneously. The lithium grand potential phase diagrams of Li-O-X and Li-O-Cl-Br suggested the forming of Li_2O and LiX at high μ_{Li}. As is known to all, the Li_2O and LiF are main SEI components in liquid organic electrolytes and they are proven to be Li-ion conductors [153,154]. Therefore, the Li_2O and LiX compound may form a SEI-type layer between anode and Li_3OX. When the potential μ_{Li} was lower than -2.9 eV, Li_3OCl began to appear as the oxygen-containing phase. At even lower μ_{Li} (-3.2 eV), Li_3OCl decomposed to Cl_2 and ClO_2. Chen et al. [104] investigated the stability of Li_3OCl using a harmonic

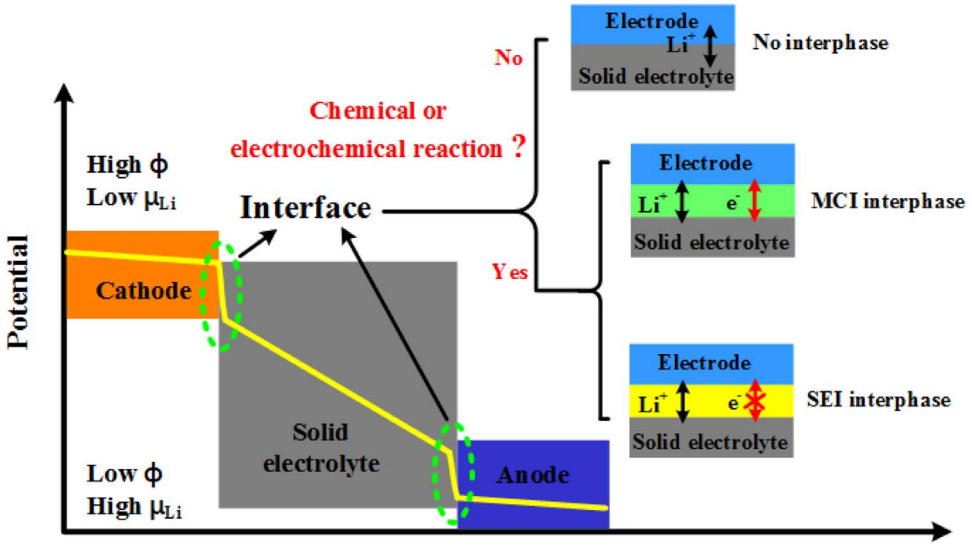

Fig. 9. Schematic diagram of cathode-ISE-anode interface and three types of interface. Types of ISE/electrode interfaces: non-reactive and no interphase; reactive and MIC interphase; and reactive and metastable SEI interphase.

phonon model. They found that Li_3OCl was mechanically unstable to octahedral rotations. Structures involving octahedral tilts had lower energy than cubic $Pm\bar{3}m$, and Li_3OCl was indeed stabilized by vibrational entropy at temperatures lower than 480 K.

Recently, Ceder et al. [155] developed a computational methodology including grand potential phase diagrams using pymatgen software package and DFT software package to examine the thermodynamics of ISEs. The predicted formation of the interphases agreed well with experimental results. They found thiophosphate electrolytes had especially high reactivity towards high voltage cathodes and a narrow electrochemical stability window. They tabulated the stability and predicted the interphases for a wide range of ISEs, coating, and electrode materials, and provided a number of high-performing combinations. Using this methodology, the decomposition reactions between spinel cathode and electrolytes (LATP and LLZO:Ta) were theoretically predicted [156]. These results are a valuable resource for researchers to find stable cathodes to improve performance in solid-state batteries with electrolytes bonded to cathodes.

Furthermore, temperature and the lithium/oxygen partial pressure are crucial process parameters to obtain high-quality ISEs. Kanno et al. [157] constructed the phase diagram for the quasi-binary Li_4GeS_4-Li_3PS_4 system including LGPS. The end-member Li_4GeS_4 has a compositional range of $0 < k < 0.3$ in $[(1\text{-}k)Li_4GeS_4 + kLi_3PS_4]$, while the other end-member γ-Li_3PS_4 has no solid solution range. Hupfer et al. [158] suggested LATP has high stability against water, allowing water based production processes. In LATP, as the substitution level of Al increasing, LATP loses rhombohedral structure because of differences in ion size and valence. Duan and Liu et al. [159] suggested that LLZO show good air stability by sintering LLZO pellets in Pt crucibles and alumina crucibles. The air stability is directly correlated with the formation of Li_2CO_3 after long time air exposure. The phenomena were also supported by other researchers [160,161].

3.2. Interfacial stability between ISEs and electrodes

The interfacial structure between ISEs and electrodes is a key factor for electrochemical performances of ASSLBs, such as rate capability, coulombic efficiency, and cycle stability, due to interfacial resistance [162,163]. Generally, high interfacial resistance has the following reasons: (i) poor interfacial contact; (ii) interfacial degradation by element mutual diffusion; (iii) impediment of ion diffusion by space charge layer; (iv) interfacial stress induced by volume change; (v) decomposition at the interface. For ASSLBs, there are several methods to enhance the ionic conductivity of the interface: (i) enlarging contact area through experimental fabrication, such as softening glassing; (ii) modulating materials' morphology, such as porous garnet ISE interface structure [164]; (iii) modifying ISE/electrode interface by coating material, such as Al_2O_3 [165]. In addition, as the definition by Wenzel et al. [166], there are three different types of interfaces based on the interphase properties (Fig. 9): (i) the stable interface with no decomposition or interphase layers; (ii) the interface formed mixed ionic/electronic conducting interphase (MCI); (iii) the interface formed with stable SEI. Moreover, typical application examples for the ISEs in ASSLBs are reviewed in Table 3. As shown in the table, the interfacial resistance and stability in ASSLBs receive extensive attention. The coating of ISEs or electrodes, adopting bilayered ISEs, and optimization of interfacial structure to improve the interfacial stability and decrease the interfacial resistance have been widely studied.

3.2.1. Interface between ISEs and anodes

For the anode side, Li-metal electrode is desired for ASSLBs with high energy density. For LISICON-like structures, earlier study suggested that LGPS was stable against Li-metal anode because only currents corresponding to lithium deposition and dissolution were found in CV measurements [32]. However, conflicting studies reported that LGPS was indeed reduced by Li-metal, forming Li_2S [167,168]. For this question, Zeier and Janek et al. [169] analyzed the interface using in-situ XPS combined with time resolved electrochemical measurements. They found the decomposition of LGPS led to the formation of interphases composed of Li_3P, Li_2S, and Li-Ge alloy (Fig. 10a). Hirayama et al. [170] reported an all-solid-state Li-ion battery including $LiNi_{0.5}Mn_{1.5}O_4$ (LNMO) cathode, LGPS ISE, and Li-metal anode. They suggested a SEI-like layer containing Li_2S was formed at LGPS/Li-metal side, which could suppress the further decomposition of LGPS. The same interphase (Li_2S) was also formed between $Li_7P_3S_{11}$ and Li-metal [171]. The theoretical calculations from DFT suggested that LGPS was reduced to Li_2S, Li_3P, and $Li_{15}Ge_4$ at a low potential and was oxidized to P_2S_5, S, and GeS_2 at high potentials [35]. Recently, Jung et al. [167] confirmed that the structure of LGPS was altered even at 0.6 V (vs. Li/Li^+), most likely forming an Li_2S phase, which explained significant degradation in the cycling of TiS_2/LGPS/Li-In solid-state batteries. The poor chemical stability of ISEs with Li-metal was also found in Li_4SnS_4 because of the reduction of tin [172]. In order to address this issue, two methods may be used: (i) modifying the surface of ISEs or passivating the Li-metal electrode; (ii) alloying Li-metal to produce Li-M (M = In, Si, and Al et al). Liang et al. [172]

Table 3.
Reported all-solid-state lithium batteries.

ISE	Cathode	Anode	Purpose	Specific effort or finding	Ref.
LISICON-like					
LSPSCl	$LiNbO_3$-coated $LiCoO_2$@AB	$Li_4Ti_5O_{12}$@AB	Suppressing ISE decomposition	Coating	[43]
LGPS	$LiNbO_3$-coated $LiCoO_2$@AB	$Li_4Ti_5O_{12}$@AB		Coating	[43]
$Li_{9.6}P_3S_{12}$	$LiNbO_3$-coated $LiCoO_2$@AB	$Li_4Ti_5O_{12}$@AB		Coating	[43]
LGPS	rGO@S@AB	Li-metal	Reducing interface resistance and stress/strain of sulfur cathodes	Coating	[214]
LGPS@doped Li_3PS_4	rGO@S@AB	Li-metal	Suppressing ISE decomposition	Bilayer ISEs design	[214]
LGPS@ $Li_7P_3S_{11}$	Cu_2ZnSnS_4/GP	Li-metal	Suppressing ISE decomposition	Bilayer ISEs design	[3]
$Li_7P_3S_{11}$	Co_9S_8@$Li_7P_3S_{11}$	Li-metal	Decreasing interfacial resistance	Interfacial architecture	[16]
LGPS	$LiNbO_3$-coated $LiCoO_2$	In-Li alloy	Suppressing ISE decomposition	Coating and alloying	[215]
LGPS	$LiNbO_3$-coated $LiNi_{0.5}Mn_{1.5}O_4$@AB	Li-metal		Coating	[170]
NASICON-like					
LATP	LATP modified $LiCoO_2$	Li-metal	Suppressing side reaction at the interface	Modifying LCO	[216]
$LiZr_2(PO_4)_3$	$LiFePO_4$	Li-metal	Testing interface stability	Self-passivation	[217]
Polymer@ LATP	$LiFePO_4$	Li-metal	Suppressing dendrite growth	Interfacial architecture	[218]
Pervoskite					
LLTO	$LiCoO_2$	$Li_4Mn_5O_{12}$	Decreasing internal resistance	Honeycomb structure of LLTO	[219]
Li_3OCl	Li-metal	Li-metal	Testing film conductivity and stability	ISE Films enhancing conductivity	[220]
Li_2OHCl	Li-metal	Li-metal	Testing stability against Li-metal	Self-passivation	[109]
$Li_2(OH)X$ (X=Cl, Br)	Polymer@$LiFePO_4$@C	Polymer@ Li-metal	Suppressing ISE decomposition	Substitution of OH^- by F^-	[108]
Garnet					
Si@LLCZN	Li-metal	Li-metal	Decreasing interfacial resistance	Coating ISE	[182]
Al_2O_3@LLCZN	Li-metal	Li-metal	Decreasing interfacial resistance	Coating ISE	[183]
LLZO	Nb@$LiCoO_2$	Li-metal	Decreasing interfacial resistance	Coating LCO	[198]
LLZO	Li_3BO_3@$LiCoO_2$	Li-metal	Suppressing the phase transition at $LiCoO_2$ side	Coating LCO	[199]
LLZO	$LiFePO_4$	Li-metal	Testing the effect of humid air	Forming insulating layer at grain boundary	[221]

Reduced graphene oxide (rGO), acetylene black (AB), and graphene (GP).

found that $3LiBH_4$·LiI was a good protective coating layer for Li_4SnS_4 to improve its compatibility with Li-metal. Li-In alloy with a charge/discharge mechanism involving alloying and de-alloying ($xLi^+ + xe^- + M \rightarrow Li_xM$) and a flat voltage plateau (0.62 V) was mostly used [173]. This is because when the In-coated ISEs contact Li-metal, the alloying process occurs between surface In- and Li-metal anode which spontaneously "seals" the In/Li interface. Therefore, resistances existing at both the In/ISE and In/Li interfaces were lowered.

Furthermore, spatially resolved EELS combined with STEM found an interphase layer between LiPON and Si anode [174]. NASICON-type structure LATP and LAGP undergoe degradation reactions at the LAMP/Li-metal interface by forming MCI interphase [175]

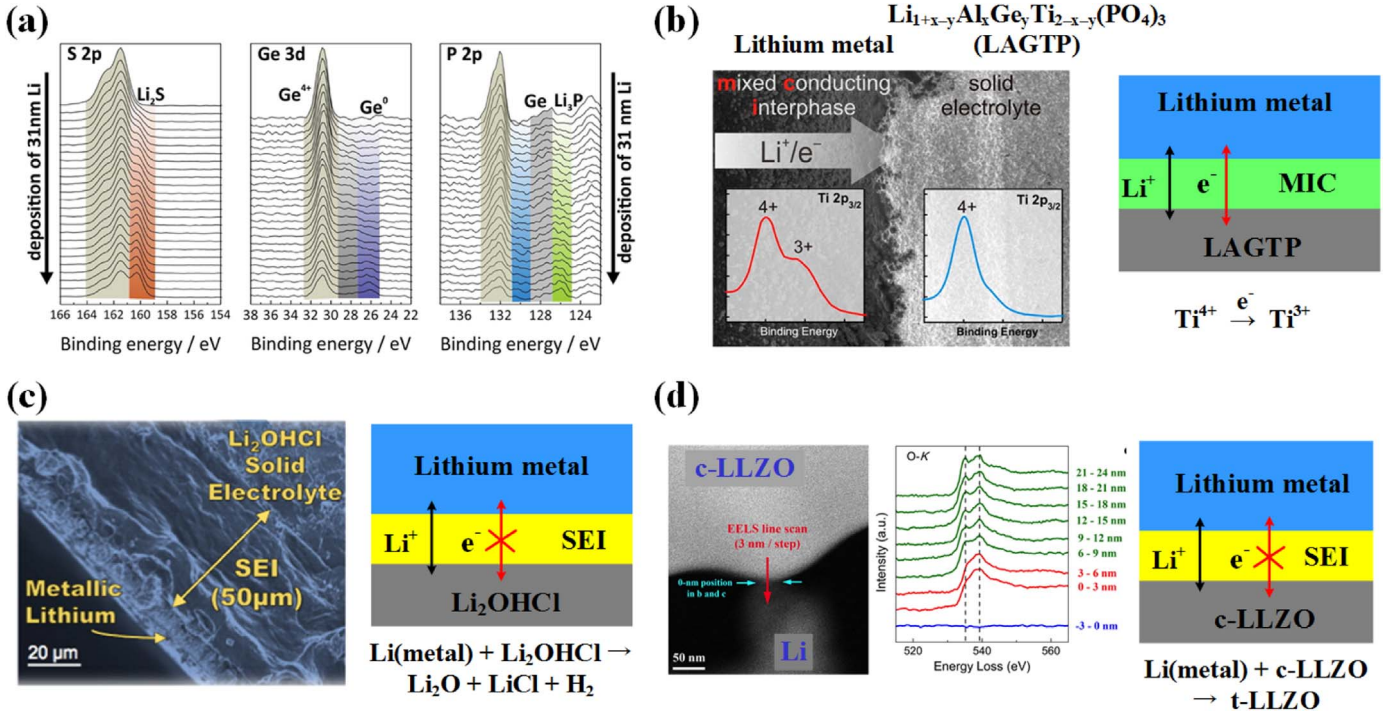

Fig. 10. (a) XPS spectra for $Li_{10}GeP_2S_{12}$ deposited on Li-metal. The identified species are marked and labeled in the spectra [169]. (b) SEM cross-section image of a LATGP sample after approximately 12 h contact with Li-metal [175]. (c) SEM of interface between Li_2OHCl and metal Li [109]. (d) Schematic illustration of the observed interface behavior when c-LLZO is contacted with Li-metal [178].

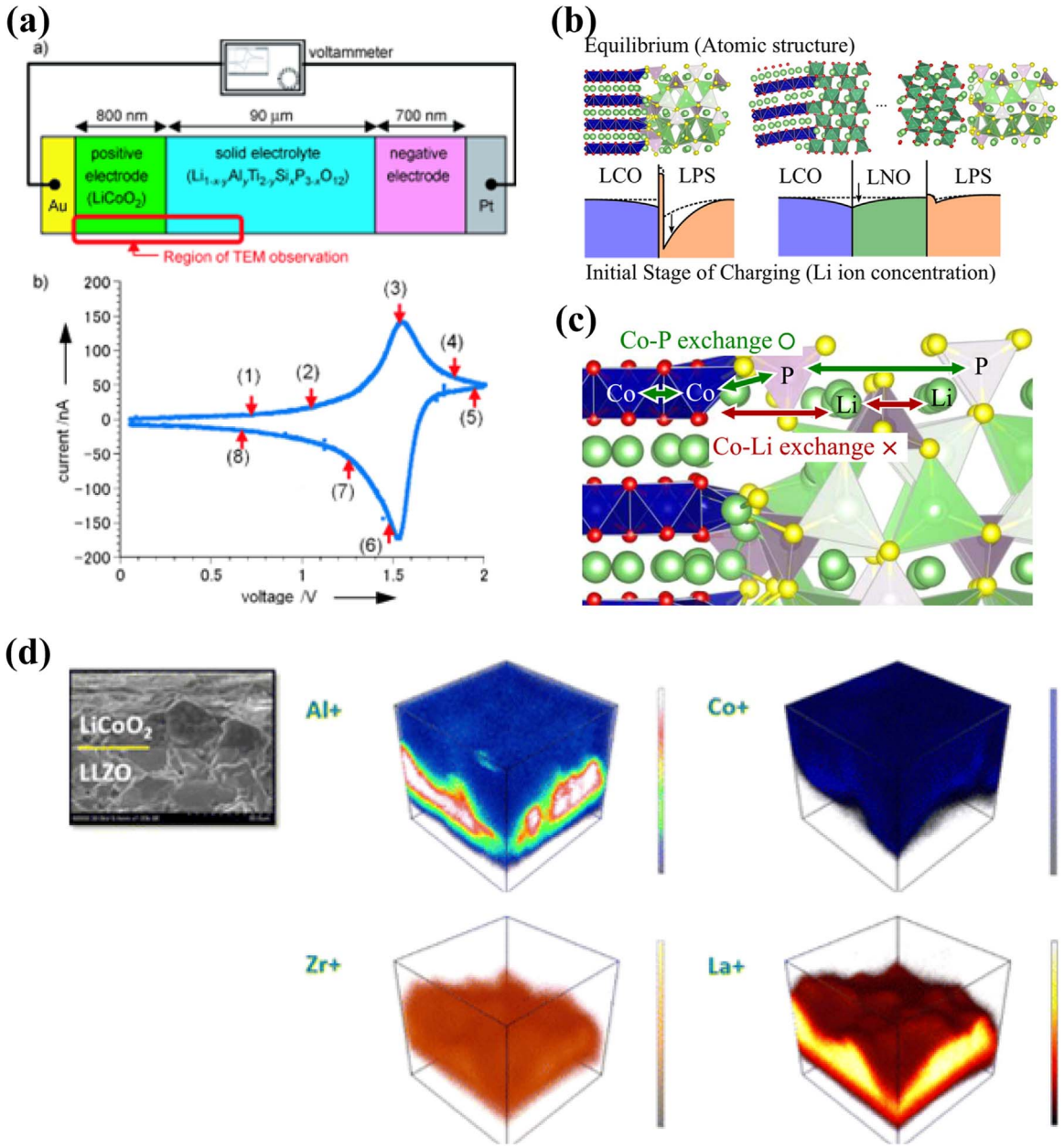

Fig. 11. (a) Macromeasurement of the battery reaction [184]. Top: schematic illustration of the sample, and bottom: initial Li-insertion/extraction reaction of the LATSPO/Pt half cell at 3.0–1.5 V (vs. Li^+/Li). (b) Schematic illustrations of interfacial Li concentration for the LCO/LPS and LCO/LNO/LPS interfaces [185]. (c) Schematic of the Li-ion mutual diffusion at $LiCoO_2$/LPS interface [194]. (d) Interphases for TOF-SIMS-enabled three-dimensional elemental maps of the $LiCoO_2$/LLZO interface [199].

(Fig. 10b). In the case of $Li_{0.35}La_{0.55}TiO_3$, Wenzel et al. [166] found the formation of reduced titanium ions and/or metal using photoelectron spectroscopy. Perovskite and anti-perovskite electrolytes are instable with Li-metal, where an apparent interfacial reaction occurs between ISEs and Li-metal [103]. Liang et al. [109] showed that the Li_2OHCl formed a stable SEI-like layer at Li-metal anode side (Fig. 10c). Li_2OHCl reacted with metallic lithium to form Li_2O and LiCl enabling the Li/Li_2OHCl/Li symmetric cell to cycle hundreds of times. Li et al. [108] studied the $Li_2(OH)_{0.9}F_{0.1}Cl$ solid electrolyte in an all solid state Li/$LiFePO_4$ battery. $Li_2(OH)_{0.9}F_{0.1}Cl$ solid electrolyte showed good cyclability and a high coulombic efficiency over 40 charge and discharge cycles.

Cubic garnet LLZO is believed to have an excellent stability but poor contact with Li-metal anode [176,177]. Recently, the stability of LLZO/Li interface was challenged by Chi et al. [178]. They found a t-LLZO interphase between c-LLZO and Li-metal using the EELS associated with in-situ STEM. The t-LLZO interphase could effectively prevent further interfacial reactions while maintained a facile ionic conductivity (Fig. 10d). Moreover, to reduce the interfacial resistance at the LLZO/Li-metal interface, sintering with an appropriate amount of Al_2O_3 [179] and porous-interface-engineering of LLZO/Li-metal to densify LLZO ISE [164,179] were developed. Afyon and Rupp et al. [164] studied the effects of electrode/electrolyte interfacial microstructures using $Li_{6.25}Al_{0.25}La_3Zr_2O_{12}$. They found porous garnet ISE interface structure enhanced Li-ion transfer at electrode/electrolyte interface. Sudo et al. [180] found Li/LLZTO/Li cells showed a “short circuit” after polarization under a current density of 0.5 mA cm^{-2} [180]. The short circuiting was due to lithium dendrite formation. Recently, Ren et al. [181] found Li/LLZTO/Li cells also showed the short-circuiting phenomena after polarization. They directly observed the Li dendrite inside LLZTO using SEM micrographs, questioning the stability of LLZO/Li interface and the effectiveness of garnet ISEs in preventing Li

dendrite growth. More studies are needed to confirm these findings as these findings are from SEM analyses. In addition, to improve the wettability of LLZO with Li-metal, Wachsman and Hu et al. [182] coated an ultrathin layer of amorphous Si over $Li_{6.85}La_{2.9}Ca_{0.1}Zr_{1.75}Nb_{0.25}O_{12}$ (LLCZN). This coating layer changes the Nb and Ca double-doped LLZO from "super-lithiophobicity" to "super-lithiophilicity". Lithiated Si acts as a Li-ion conductor layer and supporting role, which reduce the interfacial resistance and enhance interfacial stability. Later, they coated ultrathin Al_2O_3 film over LLCZN by atomic layer deposition [183]. The lithiated $Li_xAl_yO_z$ enables both good stability and wettability of Li-metal in contact with the garnet electrolyte surface and allows effective Li-ion transport.

3.2.2. Interface between ISEs and cathodes

The interface between ISEs and cathodes was also studied recently. Kazuo et al. [184] directly observed the electric potential distribution at $LiCoO_2/Li_{1+x+y}AlyTi_{2-y}SixP_{3-x}O_{12}$ (LCO/LATSPO) interface (Fig. 11a) during charge-discharge process using quantitative electron holography within TEM. Li-ion diffusion at the interface led to a steep potential drop near the interface and a gradually extended slope in solid electrolyte, which suggested that resistance was mainly contributed by the area near the interface. Hirayama et al. [170] reported decomposition products formed at the LGPS/acetylene-black interface, which could restrict the conduction of electrons and/or Li-ions in the cathode. Takada et al. [185] studied the $LiCoO_2$/LPS interface and found Li-ions at the electrolyte side of interface were depleted because of large difference in chemical potentials between LCO and LPS electrolytes, which decreased Li-ion conductivity. They adopted the SCL theory to explain the above phenomenon (Fig. 11b) [186,187]. The SCL theory was evident by the potential slope at the initial stage of charging in the voltage profile. Later, they found coating LCO using electron-insulating and ion-conducting oxide materials such as $LiNbO_3$ [188], $Li_4Ti_5O_{12}$ [185], and TaO_3 [189] as a buffer layer could suppress the formation of a space charge layer and decrease interfacial resistance.

Except for the SCL theory, some authors suggested that the cause of interfacial resistance might be ascribed to the formation of a defective layer induced by chemical reactions and mutual diffusion at the interface [190–192]. Also at the LCO/LPS interface, the defective layer and the mutual diffusion of Co were observed by TEM [193]. Recent theoretical work [194] (Fig. 11c) calculated exchange energies at LCO/LPS interface and revealed that the Co ↔ P exchange energies and Co ↔ Nb exchange energies were negative (thermodynamically favorable) and positive (thermodynamically unfavorable), respectively. A lower interfacial state in the energy gap occurred after Co ↔ P exchange, which further stabilized the Co ↔ P exchange. The $LiNbO_3$ (LNO) buffer layer suppressed such mixing because the exchange of Co and Nb was energetically unfavorable. The electronic conductive (NiS or CoS) coating on LCO also improved the electrochemical performance of cathode [192]. Other authors suggested poor performance of bare LCO was ascribed to structural degradation originating from mutual diffusion of elements at the interface [193]. Woo et al. [195] reported a uniform nanoscale Al_2O_3 layer deposited on LCO could also benefit the cyclic performance of solid state battery by reducing the formation of an interfacial layer.

For cathode/garnet interface, interfacial resistance is critical. Miara et al. [196] calculated reaction energy for LLZO against LCO, $LiMnO_2$ (LMO), and $LiFePO_4$ (LFP) over a voltage range of 0–5 V vs. Li/Li^+ using DFT method. The results indicated that LLZO/LCO was the most stable while LLZO/LFP was the most reactive, forming Li_3PO_4, $La_2Zr_2O_7$, $LaFeO_3$, and Fe_2O_3. However, these results have not been confirmed by experiments. Various methods, such as doping or elemental substitution [197], growing a thin layer (amorphous Li-Nb-O) over garnet [198] and fusing cathode and garnet together [199] were used to minimizing interfacial resistance. Yasutoshi et al. [198] decreased the LLZO/LCO interfacial resistance by introducing a thin Nb layer (~ 10 nm) at this interface, which dramatically improves cycle stability and rate capability. The Nb layer could restrict element mutual diffusion at the interface. Goodenough et al. [199] studied the interface between LCO and LLZO (Fig. 11d). They found high-temperature process for fusing LCO and LLZO induced cross-diffusion of elements and formation of low conductivity t-LLZO phase at the interface. This phase transition is a result of Al depletion in c-LLZO since Al can stabilize cubic LLZO. By introducing the Li_3BO_3 into LCO/c-LLZO interface, the coated layer could restrict Al diffusion from c-LLZO to LCO and enhance interface stability. Thermal process also induced unfavorable products between high voltage spinel cathode materials ($Li_2XMn_3O_8$, X = Ni, Fe, and Co) and ISEs ($Li_{1.5}Al_{0.5}Ti_{1.5}(PO_4)_3$ and $Li_{6.6}La_3Zr_{1.6}Ta_{0.4}O_{12}$) [156]. For the spinel materials plus electrolytes mixtures, thermal decomposition occurred forming insulating phases at temperatures above 550-600 °C. Thus, high temperature co-sintering formed dense cathode composites between spinel cathodes and oxide electrolytes resulted in products with high interfacial impedance.

4. Conclusions and perspectives

In this review, we concentrate on the ionic conductivity and stability of ISEs by discussing defect chemistry, ion-doping or elemental substitution, ion-transport mechanism, phase stability and interfacial stability in four representative inorganic solid electrolytes (LISICON-like, NASICON-like, perovskite/anti-perovskite and garnet). We highlight the roles that advanced measurement techniques and computational methods play in studies of ion-transport mechanism and interfacial stability. We review the general illustration of structures and fundamental features important to ionic conductivity or stability. Through the literature review in this field, we summarize some general design principles of ISEs and bring forward possible research directions for ISEs.

4.1. Common features of Li-ion transport mechanism

These atomic-scale investigations in Section 3 allow us to gain valuable insights into the relationship between structure and ion-transport property in LISICON-like ISEs. Four important common features are suggested as follows.

i) The first indication that Li-ion diffusion prefers through a co-operative migration mechanism via interstitialcy or vacancy. In L_3PS_4, the formation of interstitial Li-ion is energetically favorable, and cooperative migration is via interstitialcy. In LLZO, cooperative migration is suggested by theoretical studies, and the Li-ion migration is via Li vacancy because many Li-ion vacancies exist in lattice sites. One Li-ion hopping easily induces a large volume-expansion/contraction-strain during Li-ion migration, which is greater than for cooperative migration because of steric reasons. The volume-expansion/contraction-strain affects potential energy surface, which leads to different energy barriers. Recently, Recently, Mo et al. [200] suggest that Li-ions occupying high-energy sites can activate cooperative migration with a reduced migration energy barrier. During the cooperative migration of multiple ions, the Li-ions located at the high-energy sites migrate downhill, which cancels out a part of the energy barrier felt by other uphill-climbing Li-ions. Yi Cui, professor of materials science and engineering of Stanford University, commented this work offers a new and important insight on fast ion transport and provides new materials principles for finding the new solid electrolyte. Gerbrand Ceder, Professor at UC Berkeley commented that this work provides another important step forward in understanding the origin of the very high Li conductivity in some solids, as it highlights the importance of high Li content in the material leading to more concerted motion.

ii) The arrangement and composition of skeleton units in ISE structures, such as PS_4 in LISICON-like, TiO_6 in NASICON-like and perovskite, ZrO_6 in garnet, are related to ion-transport dimensionality and ionic conductivity because of uniform and/or nonuniform potential energy surface. Uniformed polynaion arrangement easily restrict the Li-ions diffusion to a frame and cause anisotropic diffusion in ISEs. Doping in XS_4 units in LISICON-like structure, especially anion-doping, helps to modify the orientation of XS_4 units and the arrangement of S atoms along Li-ion paths, and thus alters the potential energy surface, which allows considerable local oscillation and/or local Li-ions hopping to occur between lattice and interstitial sites. Li-ion diffusion is highly anisotropic in L_3PS_4 and LXPS with uniform PS_4 and/or XS_4 units. Li-ions occupy a much more uniform set of potential wells, and Li-ions diffusion occurs along *ac*-plane in β-Li_3PS_4 and along *c*-axis in LXPS, respectively. O-dopant in L_3PS_4 cause mixed PS_3O unit to show a transition from 2D diffusion to 3D with lower energy barrier. In Cl-doped LXPS, SiS_3Cl and/or PS_3Cl units help to modify the potential energy surface, which promotes the mobility of Li-ions and changes Li-ions dimensionality from 1D to 3D.

iii) The energy barrier of Li-ion migration is positive correlation with bottleneck of Li-ion diffusion pathway. Increasing the size of Li-ion conduction pathway within LISICON-like structure increases ionic conductivity and lowers energy barrier of Li-ion migration.

iv) The Li-ion mobility positive correlation with the disorder of Li-ion sublattice and the polarizability and bonding character of host atoms in the framework. In garnet ISEs, compared to Li-O tetrahedron, disordered Li-O octahedron allows Li-ions to disassociate more easily. Compared to O-atom of skeleton units, the S-atom is weakly bonded with Li-ion. These make medium Li/vacancy or Li/interstitial ratio and help Li-ions to diffusion. The mobile Li-ions and weak chemical bonds, on the other hand, lead to less chemically stable for ISEs. This creates a dilemma in designing solid electrolyte materials.

Last but not least, most of the four features are left for quantitative analyses. For example, ion-doping or elemental substitution has a broad influence on the properties of ISEs, such as ionic conductivity (Li-ion content, Li-ion distribution, migration pathway, migration bottleneck size, grain boundary conductivity, etc.), structure (microstructure, lattice volume, interface structure, etc.), and stability (phase stability, chemical stability, and electrochemical stability). Li-ion cooperative transport easily exists in ISEs with disordered Li-ion sublattice. Some evidences suggest grain boundaries are fast ion transport pathways and surface microstructure is critically important to Li-ion transport at the interface. Modeling surface structure, interfacial structures, grain boundaries structures, and nanoporous structures will be more and more important in revealing many questions in ion transport and interfacial stability. These features of Li-ion transport mechanism are needed in future experimental and theoretical works.

4.2. Comments and research directions on four type ISEs

LISICON-like ISEs are promising solid electrolytes for ASSLBs because of their high ionic conductivity and intimate solid/solid contacts. However, their chemical and electrochemical stability is the biggest problem. How to improve the interfacial stability of electrodes/LISICON-like ISEs is very important. Choosing low electric potential anode electrodes, such as Li-In alloy (electric potential is about 0.6 V), can ease or inhibit the reduction of LISICON-like ISEs. Introducing artificial buffer layer between electrodes and LISICON-like ISEs, such as $LiNbO_3$, forms stable interfacial layer with low resistance to enhance the performance of ASSLBs. LISICON-like ISEs with multiple polyanios, such as $Li_3PS_{4-x}Cl_x$ and $Li_3PS_{4-x}O_x$, can enhance their chemical stability.

LATP or LAGP in NASICON-like ISEs is promising candidate if the reduction of constituent Ti by Li-metal in the battery can be suppressed by the improvement of anodes or by controlling interfacial layer between the anode and the ISE. Furthermore, the wettability and compactness of NASICON-like ISEs are poor, which causes high interfacial and GB resistances. Thus, how to improve these two aspects, are also essential in enabling the applications of LATP or LAGP.

For perovskite LLTO ISE, the poor stability and low GB conductivity are key issues. Studies of ion-transport mechanism at grain boundary are important for the design and optimization of LLTO. Li_3OX anti-perovskite is a potential ISE due to its high ionic conductivity. But Li_3OX is thermodynamically metastable and may decompose to Li_2O and LiX. In addition, the understanding of ion-transport mechanism at bulk and grain boundary is helpful in revealing the structures of Li_3OX interfaces and developing relevant models and theories.

In garnet-type ISEs, c-LLZO is the most promising material for ASSLBs. Doping strategy is important for tuning ionic conductivity of LLZO. The substitution at Li, La, and Zr sites is related to Li-ion sites, vacancy arrangement, and other corresponding microstructures (such as volume of Li-ion migration pathway and lattice parameters). Deep understanding effects of various dopants or defects on bulk and GB conductivity is vital for optimization of LLZO ISE. More efforts on the wettability and interfacial properties are needed in the future.

Rational design of efficient electrodes/ISEs interfaces to improve their stability and decrease the interfacial resistance is one of the biggest challenges in enabling ASSLBs. The progresses in interfacial preparation techniques, such as modification of interfacial microstructure, optimum of interfacial architecture, surface coating, etc., are key factors towards the success of ASSLBs. In-situ or ex-situ passivation layers with good ionic conduction and electronic insulation can be used to stabilize the ISE/electrode interfaces. Some ISEs seemly have good interfacial stability with electrodes, but are not necessarily their intrinsic properties. The kinetics of decomposition reactions usually sluggish or interphases have good electronic insulation similar to SEI.

The use of high-through computational methods help to screen various candidates for ISE materials. The development of high-through calculations need suitable models and metrics to identify fast ion conductors. Structural stability, chemical stability, ionic conductivity, and electronic conductivity also need to be taken into careful consideration.

In conclusion, the optimization and discovery of high-performance ISEs are critical to ASSLBs. The advances of ASSLBs depend on gaining a better understanding of the fundamental science in current ISEs and exploring new ISEs. Lots of studies by advanced techniques and computational methods will be carried out on the synthesis-structure-property correlation for various ISEs. We believe that computational methods will play an increasingly significant role in charactering and predicting the structures and properties of ISEs, which promote the development of ISEs much in the near future.

Acknowledgements

This work was financially supported by the National Materials Genome Project (2016YFB0700600), the Guangdong Innovation Team Project (No. 2013N080), and the Shenzhen Science and Technology Research Grants (Nos. JCYJ20150626110958181, JCYJ20150518092933435, JCYJ20160531141048950), Chinese government under the "Thousand Youth Talents Program", Zhejiang Province Science Fund for Distinguished Young Scholars (Project LR16B060001).

Appendix A. Supporting information

Supplementary data associated with this article can be found in the online version at http://dx.doi.org/10.1016/j.ensm.2017.08.015.

References

[1] V. Thangadurai, S. Narayanan, D. Pinzaru, Chem. Soc. Rev. 43 (2014) 4714–4727.
[2] J.C. Bachman, S. Muy, A. Grimaud, H.-H. Chang, N. Pour, S.F. Lux, O. Paschos, F. Maglia, S. Lupart, P. Lamp, L. Giordano, Y. Shao-Horn, Chem. Rev. 116 (2016) 140–162.
[3] H. Wan, G. Peng, X. Yao, J. Yang, P. Cui, X. Xu, Energy Storage Mater. 4 (2016) 59–65.
[4] Y. Wang, W.-H. Zhong, ChemElectroChem. 2 (2015) 22–36.
[5] R. Chen, W. Qu, X. Guo, L. Li, F. Wu, Mater. Horiz. 3 (2016) 487–516.
[6] Y. Xiayin, H. Bingxin, Y. Jingyun, P. Gang, H. Zhen, G. Chao, L. Deng, X. Xiaoxiong, Chin. Phys. B 25 (2016) 018802.
[7] S. Lee, S.S. Park, J. Phys. Chem. C 116 (2012) 6484–6489.
[8] M.S. Islam, D.J. Driscoll, C.A.J. Fisher, P.R. Slater, Chem. Mater. 17 (2005) 5085–5092.
[9] Y. Yang, Q. Wu, Y. Cui, Y. Chen, S. Shi, R.-Z. Wang, H. Yan, ACS. Appl. Mater. Interfaces 8 (2016) 25229–25242.
[10] S. Shi, P. Lu, Z. Liu, Y. Qi, L.G. Hector, H. Li, S.J. Harris, J. Am. Chem. Soc. 134 (2012) 15476–15487.
[11] S. Shi, Y. Qi, H. Li, L.G. Hector, J. Phys. Chem. C 117 (2013) 8579–8593.
[12] Y. Wang, W.D. Richards, S.P. Ong, L.J. Miara, J.C. Kim, Y. Mo, G. Ceder, Nat. Mater. 14 (2015) 1026–1031.
[13] H.Y.P. Hong, Mater. Res. Bull. 13 (1978) 117–124.
[14] R. Kanno, T. Hata, Y. Kawamoto, M. Irie, Solid State Ion. 130 (2000) 97–104.
[15] B. Huang, X. Yao, Z. Huang, Y. Guan, Y. Jin, X. Xu, J. Power Sources 284 (2015) 206–211.
[16] X. Yao, D. Liu, C. Wang, P. Long, G. Peng, Y.-S. Hu, H. Li, L. Chen, X. Xu, Nano Lett. 16 (2016) 7148–7154.
[17] Z. Lin, Z. Liu, N.J. Dudney, C. Liang, ACS Nano 7 (2013) 2829–2833.
[18] K. Homma, M. Yonemura, T. Kobayashi, M. Nagao, M. Hirayama, R. Kanno, Solid State Ion. 182 (2011) 53–58.
[19] Z. Liu, W. Fu, E.A. Payzant, X. Yu, Z. Wu, N.J. Dudney, J. Kiggans, K. Hong, A.J. Rondinone, C. Liang, J. Am. Chem. Soc. 135 (2013) 975–978.
[20] M. Gobet, S. Greenbaum, G. Sahu, C. Liang, Chem. Mater. 26 (2014) 3558–3564.
[21] K. Ohara, A. Mitsui, M. Mori, Y. Onodera, S. Shiotani, Y. Koyama, Y. Orikasa, M. Murakami, K. Shimoda, K. Mori, T. Fukunaga, H. Arai, Y. Uchimoto, Z. Ogumi, Sci. Rep. 6 (2016) 21302.
[22] N.D. Lepley, N.A.W. Holzwarth, Y.A. Du, Phys. Rev. B 88 (2013) 2991–3000.
[23] R. Xiao, H. Li, L. Chen, Sci. Rep. 5 (2015) 14227.
[24] C. Müller, E. Zienicke, S. Adams, J. Habasaki, P. Maass, Phys. Rev. B 75 (2007) 014203.
[25] J. Gao, G. Chu, M. He, S. Zhang, R. Xiao, H. Li, L. Chen, Sci. China Phys. Mech. 57 (2014) 1526–1536.
[26] I.D. Brown, Chem. Rev. 109 (2009) 6858–6919.
[27] S. Adams, J. Swenson, Solid State Ion. 154–155 (2002) 151–159.
[28] S. Adams, J. Power Sources 159 (2006) 200–204.
[29] S. Adams, Solid State Ion. 177 (2006) 1625–1630.
[30] X. Wang, R. Xiao, H. Li, L. Chen, Phys. Chem. Chem. Phys. 18 (2016) 21269–21277.
[31] J. Yang, J.S. Tse, Comput. Mater. Sci. 107 (2015) 134–138.
[32] N. Kamaya, K. Homma, Y. Yamakawa, M. Hirayama, R. Kanno, M. Yonemura, T. Kamiyama, Y. Kato, S. Hama, K. Kawamoto, A. Mitsui, Nat. Mater. 10 (2011) 682–686.
[33] D.A. Weber, A. Senyshyn, K.S. Weldert, S. Wenzel, W. Zhang, R. Kaiser, S. Berendts, J. Janek, W.G. Zeier, Chem. Mater. 28 (2016) 5905–5915.
[34] X. Liang, L. Wang, Y. Jiang, J. Wang, H. Luo, C. Liu, J. Feng, Chem. Mater. 27 (2015) 5503–5510.
[35] Y. Mo, S.P. Ong, G. Ceder, Chem. Mater. 24 (2012) 15–17.
[36] F. Du, X. Ren, J. Yang, J. Liu, W. Zhang, J. Phys. Chem. C 118 (2014) 10590–10595.
[37] S. Nishino, T. Fujiwara, H. Yamasaki, Phys. Rev. B 90 (2014).
[38] M. Xu, J. Ding, E. Ma, Appl. Phys. Lett. 101 (2012) 031901.
[39] S. Adams, R. Prasada Rao, J. Mater. Chem. 22 (2012) 7687–7691.
[40] A. Lundén, Solid State Ion. 28 (1988) 163–167.
[41] E.A. Secco, Solid State Ion. 45 (1991) 335–336.
[42] S.P. Ong, Y. Mo, W.D. Richards, L. Miara, H.S. Lee, G. Ceder, Energy Environ. Sci. 6 (2012) 148–156.
[43] Y. Kato, S. Hori, T. Saito, K. Suzuki, M. Hirayama, A. Mitsui, M. Yonemura, H. Iba, R. Kanno, Nat. Energy 1 (2016) 16030.
[44] L.O. Hagman, P. Kierkegaard, P. Karvonen, A.I. Virtanen, J. Paasivirta, L.O. Hagman, P. Kierkegaard, P. Karvonen, A.I. Virtanen, J. Paasivirta, Acta Chem. Scand. 22 (1968) 1822–1832.
[45] M. Alami, R. Brochu, J.L. Soubeyroux, P. Gravereau, G. Le Flem, P. Hagenmuller, J. Solid State Chem. 90 (1991) 185–193.
[46] D.T. Qui, S. Hamdoune, J.L. Soubeyroux, E. Prince, J. Solid State Chem. 72 (1988) 309–315.
[47] K. Arbi, M. Ayadi-Trabelsi, J. Sanz, J. Mater. Chem. 12 (2002) 2985–2990.
[48] M. Catti, A. Comotti, S. Di Blas, Chem. Mater. 15 (2003) 1628–1632.
[49] J. Angenault, J.C. Couturier, J.P. Souron, D. Siliqi, M. Quarton, J. Mater. Sci. Lett. 11 (1992) 1705–1707.
[50] P. Maldonado-Manso, E.R. Losilla, M. Martínez-Lara, M.A.G. Aranda, S. Bruque, F.E. Mouahid, M. Zahir, Chem. Mater. 15 (2003) 1879–1885.
[51] R. Kahlaoui, K. Arbi, I. Sobrados, R. Jimenez, J. Sanz, R. Ternane, Inorg. Chem. (2017).
[52] K. Arbi, M. Hoelzel, A. Kuhn, F. García-Alvarado, J. Sanz, Inorg. Chem. 52 (2013) 9290–9296.
[53] G.J. Redhammer, D. Rettenwander, S. Pristat, E. Dashjav, C.M.N. Kumar, D. Topa, F. Tietz, Solid State Sci. 60 (2016) 99–107.
[54] M. Perez-Estebanez, J. Isasi-Marin, D.M. Tobbens, A. Rivera-Calzada, C. Leon, Solid State Ion. 266 (2014) 1–8.
[55] K. Arbi, M. Hoelzel, A. Kuhn, F. Garcia-Alvarado, J. Sanz, Phys. Chem. Chem. Phys. 16 (2014) 18397–18405.
[56] M. Monchak, T. Hupfer, A. Senyshyn, H. Boysen, D. Chernyshov, T. Hansen, K.G. Schell, E.C. Bucharsky, M.J. Hoffmann, H. Ehrenberg, Inorg. Chem. 55 (2016) 2941–2945.
[57] G. Nuspl, T. Takeuchi, A. Weiß, H. Kageyama, K. Yoshizawa, T. Yamabe, J. Appl. Phys. 86 (1999) 5484–5491.
[58] B. Lang, B. Ziebarth, C. Elsässer, Chem. Mater. 27 (2015) 5040–5048.
[59] H. Aono, E. Sugimoto, Y. Sadaoka, N. Imanaka, G.-y. Adachi, Chem. Lett. 19 (1990) 1825–1828.
[60] S. Duluard, A. Paillassa, L. Puech, P. Vinatier, V. Turq, P. Rozier, P. Lenormand, P.-L. Taberna, P. Simon, F. Ansart, J. Eur. Ceram. Soc. 33 (2013) 1145–1153.
[61] T. Hupfer, E.C. Bucharsky, K.G. Schell, A. Senyshyn, M. Monchak, M.J. Hoffmann, H. Ehrenberg, Solid State Ion. 288 (2016) 235–239.
[62] J.L. Narváez-Semanate, A.C.M. Rodrigues, Solid State Ion. 181 (2010) 1197–1204.
[63] F. Ma, E. Zhao, S. Zhu, W. Yan, D. Sun, Y. Jin, C. Nan, Solid State Ion. 295 (2016) 7–12.
[64] J. Kang, H. Chung, C. Doh, B. Kang, B. Han, J. Power Sources 293 (2015) 11–16.
[65] H. Aono, E. Sugimoto, Y. Sadaoka, N. Imanaka, G. Adachi, ChemInform 137 (1990) 1023–1027.
[66] D. Rettenwander, A. Welzl, S. Pristat, F. Tietz, S. Taibl, G.J. Redhammer, J. Fleig, J. Mater. Chem. A 4 (2016) 1506–1513.
[67] V. Epp, Q. Ma, E.-M. Hammer, F. Tietz, M. Wilkening, Phys. Chem. Chem. Phys. 17 (2015) 32115–32121.
[68] J. Emery, T. Šalkus, M. Barré, J. Phys. Chem. C 121 (2017) 246–254.
[69] J. Emery, T. Šalkus, A. Abramova, M. Barré, A.F. Orliukas, J. Phys. Chem. C 120 (2016) 26173–26186.
[70] E.C. Bucharsky, K.G. Schell, A. Hintennach, M.J. Hoffmann, Solid State Ion. 274 (2015) 77–82.
[71] K. Arbi, S. Mandal, J.M. Rojo, J. Sanz, Chem. Mater. 14 (2002) 1091–1097.
[72] L. Huang, Z. Wen, M. Wu, X. Wu, Y. Liu, X. Wang, J. Power Sources 196 (2011) 6943–6946.
[73] B. Kumar, D. Thomas, J. Kumar, J. Electrochem. Soc. 156 (2009) A506–A513.
[74] C.R. Mariappan, M. Gellert, C. Yada, F. Rosciano, B. Roling, Electrochem. Commun. 14 (2012) 25–28.
[75] B. Kumar, J.S. Thokchom, J. Am. Ceram. Soc. 90 (2007) 3323–3325.
[76] M. Mahmoud, Y. Cui, M. Rohde, C. Ziebert, G. Link, H. Seifert, Materials 9 (2016) 506.
[77] H. Yamada, D. Tsunoe, S. Shiraishi, G. Isomichi, J. Phys. Chem. C 119 (2015) 5412–5419.
[78] H. Aono, E. Sugimoto, Y. Sadaoka, N. Imanaka, G.-y Adachi, Solid State Ion. 47 (1991) 257–264.
[79] K. Takada, Langmuir 29 (2013) 7538–7541.
[80] K. Takada, N. Ohta, L. Zhang, X. Xu, B.T. Hang, T. Ohnishi, M. Osada, T. Sasaki, Solid State Ion. 225 (2012) 594–597.
[81] S. Stramare, V. Thangadurai, W. Weppner, Chem. Mater. 15 (2003) 3974–3990.
[82] G.-y Adachi, N. Imanaka, S. Tamura, Chem. Rev. 102 (2002) 2405–2430.
[83] Y. Inaguma, C. Liquan, M. Itoh, T. Nakamura, T. Uchida, H. Ikuta, M. Wakihara, Solid State Commun. 86 (1993) 689–693.
[84] C.W. Ban, G.M. Choi, Solid State Ion. 140 (2001) 285–292.
[85] Y. Harada, H. Watanabe, J. Kuwano, Y. Saito, J. Power Sources 81–82 (1999) 777–781.
[86] J. Wolfenstine, J.L. Allen, J. Read, J. Sakamoto, G. Gonalez-Doncel, J. Power Sources 195 (2010) 4124–4128.
[87] Y. Inaguma, M. Nakashima, J. Power Sources 228 (2013) 250–255.
[88] C. Hua, X. Fang, Z. Wang, L. Chen, Electrochem. Commun. 32 (2013) 5–8.
[89] A. Mei, X.-L. Wang, J.-L. Lan, Y.-C. Feng, H.-X. Geng, Y.-H. Lin, C.-W. Nan, Electrochim. Acta 55 (2010) 2958–2963.
[90] C. Ma, K. Chen, C. Liang, C.-W. Nan, R. Ishikawa, K. More, M. Chi, Energy Environ. Sci. 7 (2014) 1638–1642.
[91] C.H. Chen, K. Amine, Solid State Ion. 144 (2001) 51–57.
[92] M. O'Keeffe, J.-O. Bovin, Science 206 (1979) 599–600.
[93] Y. Zhao, J. Solid State Chem. 141 (1998) 121–132.
[94] Y. Zhao, D.J. Weidner, J.B. Parise, D.E. Cox, Phys. Earth Planet. Inter. 76 (1993) 1–16.
[95] A. Yoshiasa, D. Sakamoto, H. Okudera, M. Sugahara, Ki Ota, A. Nakatsuka, Z. Anorg. Allg. Chem. 631 (2005) 502–506.
[96] N. Bonanos, K.S. Knight, B. Ellis, Solid State Ion. 79 (1995) 161–170.
[97] J. Zhu, S. Li, Y. Zhang, J.W. Howard, X. Lü, Y. Li, Y. Wang, R.S. Kumar, L. Wang, Y. Zhao, Appl. Phys. Lett. 109 (2016) 101904.
[98] H. Stephen, Rep. Prog. Phys. 67 (2004) 1233.
[99] S. Hull, D.A. Keen, P.A. Madden, M. Wilson, J. Phys. : Condens. Matter. 19 (2007) 406214.
[100] Y. Zhang, Y. Zhao, C. Chen, Phys. Rev. B 87 (2013) 134303.
[101] Y. Zhao, L.L. Daemen, J. Am. Chem. Soc. 134 (2012) 15042–15047.
[102] Z. Deng, B. Radhakrishnan, S.P. Ong, Chem. Mater. 27 (2015) 3749–3755.
[103] A. Emly, E. Kioupakis, A. Van der Ven, Chem. Mater. 25 (2013) 4663–4670.
[104] Z. Lu, C. Chen, Z.M. Baiyee, X. Chen, C. Niu, F. Ciucci, Phys. Chem. Chem. Phys.

17 (2015) 32547–32555.
[105] R. Mouta, M.Á.B. Melo, E.M. Diniz, C.W.A. Paschoal, Chem. Mater. 26 (2014) 7137–7144.
[106] R. Mouta, E.M. Diniz, C.W.A. Paschoal, J. Mater. Chem. A 4 (2016) 1586–1590.
[107] G. Schwering, A. Hönnerscheid, L. van Wüllen, M. Jansen, ChemPhysChem 4 (2003) 343–348.
[108] Y. Li, W. Zhou, S. Xin, S. Li, J. Zhu, X. Lü, Z. Cui, Q. Jia, J. Zhou, Y. Zhao, J.B. Goodenough, Angew. Chem. 128 (2016) 10119–10122.
[109] Z.D. Hood, H. Wang, A. Samuthira Pandian, J.K. Keum, C. Liang, J. Am. Chem. Soc. 138 (2016) 1768–1771.
[110] O. Kwon, M. Hirayama, K. Suzuki, Y. Kato, T. Saito, M. Yonemura, T. Kamiyama, R. Kanno, J. Mater. Chem. A 3 (2015) 438–446.
[111] E.J. Cussen, Chem. Commun. 37 (2006) 412–413.
[112] H. Buschmann, J. Dölle, S. Berendts, A. Kuhn, P. Bottke, M. Wilkening, P. Heitjans, A. Senyshyn, H. Ehrenberg, A. Lotnyk, Phys. Chem. Chem. Phys. 13 (2011) 19378–19392.
[113] Y. Li, J.T. Han, C.A. Wang, H. Xie, J.B. Goodenough, J. Mater. Chem. 22 (2012) 15357–15361.
[114] K. Liu, C.-A. Wang, Electrochem. Commun. 48 (2014) 147–150.
[115] X. Tong, V. Thangadurai, E.D. Wachsman, Inorg. Chem. 54 (2015) 3600–3607.
[116] R. Inada, S. Yasuda, M. Tojo, K. Tsuritani, T. Tojo, Y. Sakurai, Front. Energy Res. 4 (2016).
[117] C. Bernuy-Lopez, W. Manalastas, J.M. Lopez del Amo, A. Aguadero, F. Aguesse, J.A. Kilner, Chem. Mater. 26 (2014) 3610–3617.
[118] J.-F. Wu, E.-Y. Chen, Y. Yu, L. Liu, Y. Wu, W.K. Pang, V.K. Peterson, X. Guo, ACS. Appl. Mater. Interfaces 9 (2017) 1542–1552.
[119] D. Rettenwander, G. Redhammer, F. Preishuberpflügl, C. Lei, L. Miara, R. Wagner, A. Welzl, E. Suard, M.M. Doeff, M. Wilkening, Chem. Mater. 28 (2016) 2384–2392.
[120] L. Buannic, B. Orayech, J.-M. López Del Amo, J. Carrasco, N.A. Katcho, F. Aguesse, W. Manalastas, W. Zhang, J. Kilner, A. Llordés, Chem. Mater. 29 (2017) 1769–1778.
[121] C.A. Geiger, E. Alekseev, B. Lazic, M. Fisch, T. Armbruster, R. Langner, M. Fechtelkord, N. Kim, T. Pettke, W. Weppner, Inorg. Chem. 50 (2011) 1089–1097.
[122] D. Wang, G. Zhong, O. Dolotko, Y. Li, M. Mcdonald, J. Mi, R. Fu, Y. Yang, J. Mater. Chem. A 2 (2014) 20271–20279.
[123] Y. Chen, E. Rangasamy, C. Liang, K. An, Chem. Mater. 27 (2015) 5491–5494.
[124] Y. Li, J.-T. Han, C.-A. Wang, S.C. Vogel, H. Xie, M. Xu, J.B. Goodenough, J. Power Sources 209 (2012) 278–281.
[125] D. Rettenwander, P. Blaha, R. Laskowski, K. Schwarz, P. Bottke, M. Wilkening, C.A. Geiger, G. Amthauer, Chem. Mater. 26 (2014) 2617–2623.
[126] D.O. Shin, K. Oh, K.M. Kim, K.-Y. Park, B. Lee, Y.-G. Lee, K. Kang, Sci. Rep. 5 (2015).
[127] L.J. Miara, S.P. Ong, Y. Mo, W.D. Richards, Y. Park, J.-M. Lee, H.S. Lee, G. Ceder, Chem. Mater. 25 (2013) 3048–3055.
[128] S. Adams, R.P. Rao, J. Mater. Chem. 22 (2012) 1426–1434.
[129] N. Bernstein, M.D. Johannes, K. Hoang, Phys. Rev. Lett. 109 (2012) 205702.
[130] Y. Chen, E. Rangasamy, C.R. dela Cruz, C. Liang, K. An, J. Mater. Chem. A 3 (2015) 22868–22876.
[131] Y. Jin, P.J. Mcginn, J. Power Sources 196 (2011) 8683–8687.
[132] R. Murugan, V. Thangadurai, W. Weppner, Appl. Phys. A 91 (2008) 615–620.
[133] M.M. Ahmad, A. Al-Jaafari, J. Mater. Sci. – Mater. Electron. 26 (2015) 1–7.
[134] M.P. O'Callaghan, E.J. Cussen, Chem. Commun. (2007) 2048–2050.
[135] M.P. O'Callaghan, A.S. Powell, J.J. Titman, G.Z. Chen, E.J. Cussen, Chem. Mater. 20 (2008) 2360–2369.
[136] R. Jalem, M.J.D. Rushton, W. Manalastas, M. Nakayama, T. Kasuga, J.A. Kilner, R.W. Grimes, Chem. Mater. 27 (2015) 2821–2831.
[137] A.K. Baral, S. Narayanan, F. Ramezanipour, V. Thangadurai, Phys. Chem. Chem. Phys. 16 (2014) 11356–11365.
[138] L. van Wullen, T. Echelmeyer, H.-W. Meyer, D. Wilmer, Phys. Chem. Chem. Phys. 9 (2007) 3298–3303.
[139] D. Wang, G. Zhong, W.K. Pang, Z. Guo, Y. Li, M.J. Mcdonald, R. Fu, J.X. Mi, Y. Yang, Chem. Mater. 27 (2015) 6650–6659.
[140] Y. Wang, A. Huq, W. Lai, Solid State Ion. 255 (2014) 39–49.
[141] T. Travis, S. Asma, M.D. Johannes, H. Ashfia, J.L. Allen, W. Jeff, S. Jeff, Adv. Energy Mater. 5 (2015) 150096.
[142] J. Han, J. Zhu, Y. Li, X. Yu, S. Wang, G. Wu, H. Xie, S.C. Vogel, F. Izumi, K. Momma, Chem. Commun. 48 (2012) 9840–9842.
[143] J. Awaka, A. Takashima, K. Kataoka, N. Kijima, Y. Idemoto, J. Akimoto, ChemInform 42 (2011) 60–62.
[144] M. Xu, M.S. Park, J.M. Lee, T.Y. Kim, Y.S. Park, E. Ma, Phys. Rev. B 85 (2012) 052301.
[145] R. Jalem, Y. Yamamoto, H. Shiiba, M. Nakayama, H. Munakata, T. Kasuga, K. Kanamura, Chem. Mater. 25 (2013) 425–430.
[146] R. Jalem, M. Nakayama, W. Manalastas, J.A. Kilner, R.W. Grimes, T. Kasuga, K. Kanamura, J. Phys. Chem. C 119 (2015) 20783–20791.
[147] M. Sumita, Y. Tanaka, M. Ikeda, T. Ohno, J. Phys. Chem. C 120 (2016) 13332–13339.
[148] N.D. Lepley, N.A.W. Holzwarth, Phys. Rev. B 92 (2015) 214201.
[149] F. Han, Y. Zhu, X. He, Y. Mo, C. Wang, Adv. Energy Mater. 6 (2016) 1501590.
[150] Y. Zhu, X. He, Y. Mo, ACS. Appl. Mater. Interfaces 7 (2015) 23685–23693.
[151] Y. Zhu, X. He, Y. Mo, J. Mater. Chem. A 4 (2015) 3253–3266.
[152] W.D. Richards, Y. Wang, L.J. Miara, J.C. Kim, G. Ceder, Energy Environ. Sci. 9 (2016) 3272–3278.
[153] T.W.D. Farley, W. Hayes, S. Hull, M.T. Hutchings, M. Vrtis, J. Phys.: Condens. Matter. 3 (1991) 4761.
[154] H. Yildirim, A. Kinaci, M.K.Y. Chan, J.P. Greeley, ACS. Appl. Mater. Interfaces 7 (2015) 18985–18996.
[155] W.D. Richards, L.J. Miara, Y. Wang, J.C. Kim, G. Ceder, Chem. Mater. 28 (2016) 266–273.
[156] L. Miara, A. Windmüller, C.-L. Tsai, W.D. Richards, Q. Ma, S. Uhlenbruck, O. Guillon, G. Ceder, ACS. Appl. Mater. Interfaces 8 (2016) 26842–26850.
[157] S. Hori, M. Kato, K. Suzuki, M. Hirayama, Y. Kato, R. Kanno, J. Am. Ceram. Soc. 98 (2015) 3352–3360.
[158] T. Hupfer, E.C. Bucharsky, K.G. Schell, M.J. Hoffmann, Solid State Ion. 302 (2017) 49–53.
[159] W. Xia, B. Xu, H. Duan, Y. Guo, H. Kang, H. Li, H. Liu, ACS. Appl. Mater. Interfaces 8 (2016) 5335–5342.
[160] Y. Wang, W. Lai, J. Power Sources 275 (2015) 612–620.
[161] L. Cheng, E.J. Crumlin, W. Chen, R. Qiao, H. Hou, S. Franz Lux, V. Zorba, R. Russo, R. Kostecki, Z. Liu, K. Persson, W. Yang, J. Cabana, T. Richardson, G. Chen, M. Doeff, Phys. Chem. Chem. Phys. 16 (2014) 18294–18300.
[162] K. Takada, N. Ohta, Y. Tateyama, J. Inorg. Organomet. Polym. Mater. 25 (2015) 205–213.
[163] H. Yokokawa, Solid State Ion. 285 (2016) 126–135.
[164] V.D.B. Jan, S. Afyon, J.L.M. Rupp, Adv. Energy Mater. 6 (2016) 1600736.
[165] X. Han, Y. Gong, K. Fu, X. He, G.T. Hitz, J. Dai, A. Pearse, B. Liu, H. Wang, G. Rubloff, Y. Mo, V. Thangadurai, E.D. Wachsman, L. Hu, Nat. Mater. 1 (2016) 1–9.
[166] S. Wenzel, T. Leichtweiss, D. Krüger, J. Sann, J. Janek, Solid State Ion. 278 (2015) 98–105.
[167] B.R. Shin, Y.J. Nam, D.Y. Oh, D.H. Kim, J.W. Kim, Y.S. Jung, Electrochim. Acta. 146 (2014) 395–402.
[168] Y.S. Jung, D.Y. Oh, Y.J. Nam, K.H. Park, Isr. J. Chem. 55 (2015) 472–485.
[169] S. Wenzel, S. Randau, T. Leichtweiß, D.A. Weber, J. Sann, W.G. Zeier, J. Janek, Chem. Mater. 28 (2016) 2400–2407.
[170] G. Oh, M. Hirayama, O. Kwon, K. Suzuki, R. Kanno, Chem. Mater. 28 (2016) 2634–2640.
[171] S. Wenzel, D.A. Weber, T. Leichtweiss, M.R. Busche, J. Sann, J. Janek, Solid State Ion. 286 (2016) (24-3).
[172] G. Sahu, Z. Lin, J. Li, Z. Liu, N. Dudney, C. Liang, Energy Environ. Sci. 7 (2014) 1053–1058.
[173] Y.S. Jung, K.T. Lee, J.H. Kim, J.Y. Kwon, S.M. Oh, Adv. Funct. Mater. 18 (2008) 3010–3017.
[174] D. Santhanagopalan, D. Qian, T. Mcgilvray, Z. Wang, F. Wang, F. Camino, J. Graetz, N. Dudney, Y.S. Meng, J. Phys. Chem. Lett. 5 (2013) 298–303.
[175] P. Hartmann, T. Leichtweiss, M.R. Busche, M. Schneider, M. Reich, J. Sann, P. Adelhelm, J. Janek, J. Phys. Chem. C 117 (2013) 21064–21074.
[176] K. Ishiguro, Y. Nakata, M. Matsui, I. Uechi, Y. Takeda, O. Yamamoto, N. Imanishi, J. Electrochem. Soc. 160 (2013) A1690–A1693.
[177] B. Wu, S. Wang, W.J. Evans, Iv, D.Z. Deng, J. Yang, J. Xiao, J. Mater. Chem. A 4 (2016) 15266–15280.
[178] C. Ma, Y. Cheng, K. Yin, J. Luo, A. Sharafi, J. Sakamoto, J. Li, K.L. More, N.J. Dudney, M. Chi, Nano Lett. 16 (2016) 7030–7036.
[179] L. Cheng, W. Chen, M. Kunz, K. Persson, N. Tamura, G. Chen, M. Doeff, ACS. Appl. Mater. Interfaces 7 (2015) 2073–2081.
[180] R. Sudo, Y. Nakata, K. Ishiguro, M. Matsui, A. Hirano, Y. Takeda, O. Yamamoto, N. Imanishi, Solid State Ion. 262 (2014) 151–154.
[181] Y. Ren, Y. Shen, Y. Lin, C.-W. Nan, Electrochem. Commun. 57 (2015) 27–30.
[182] W. Luo, Y. Gong, Y. Zhu, K.K. Fu, J. Dai, S.D. Lacey, C. Wang, B. Liu, X. Han, Y. Mo, E.D. Wachsman, L. Hu, J. Am. Chem. Soc. 138 (2016) 12258–12262.
[183] X. Han, Y. Gong, K. Fu, X. He, G.T. Hitz, J. Dai, A. Pearse, B. Liu, H. Wang, G. Rubloff, Y. Mo, V. Thangadurai, E.D. Wachsman, L. Hu, Nat. Mater. 16 (2017) 572–579.
[184] K. Yamamoto, Y. Iriyama, T. Asaka, T. Hirayama, H. Fujita, C.A.J. Fisher, K. Nonaka, Y. Sugita, Z. Ogumi, Angew. Chem. Int. Ed. 49 (2010) 4414–4417.
[185] N. Ohta, K. Takada, L. Zhang, R. Ma, M. Osada, T. Sasaki, Adv. Mater. 18 (2006) 2226–2229.
[186] K. Takada, N. Ohta, L. Zhang, K. Fukuda, I. Sakaguchi, R. Ma, M. Osada, T. Sasaki, Solid State Ion. 179 (2008) 1333–1337.
[187] J. Haruyama, K. Sodeyama, L. Han, K. Takada, Y. Tateyama, Chem. Mater. 26 (2014) 4248–4255.
[188] N. Ohta, K. Takada, I. Sakaguchi, L. Zhang, R. Ma, K. Fukuda, M. Osada, T. Sasaki, Electrochem. Commun. 9 (2007) 1486–1490.
[189] X. Xu, K. Takada, K. Fukuda, T. Ohnishi, K. Akatsuka, M. Osada, B.T. Hang, K. Kumagai, T. Sekiguchi, T. Sasaki, Energy Environ. Sci. 4 (2011) 3509–3512.
[190] A. Hayashi, M. Tatsumisago, Electron. Mater. Lett. 8 (2012) 199–207.
[191] K. Takada, Acta Mater. 61 (2013) 759–770.
[192] A. Sakuda, N. Nakamoto, H. Kitaura, A. Hayashi, K. Tadanaga, M. Tatsumisago, J. Mater. Chem. 22 (2012) 15247–15254.
[193] A. Sakuda, A. Hayashi, M. Tatsumisago, Chem. Mater. 22 (2010) 949–956.
[194] J. Haruyama, K. Sodeyama, Y. Tateyama, ACS. Appl. Mater. Interfaces 9 (2017) 286–292.
[195] J.H. Woo, J.E. Trevey, A.S. Cavanagh, S.C. Yong, S.C. Kim, S.M. George, K.H. Oh, S.H. Lee, J. Electrochem. Soc. 159 (2012) A1120–A1124.
[196] L.J. Miara, W.D. Richards, Y.E. Wang, G. Ceder, Chem. Mater. 27 (2015) 4040–4047.
[197] S. Narayanan, F. Ramezanipour, V. Thangadurai, Inorg. Chem. 54 (2015) 6968–6977.
[198] T. Kato, T. Hamanaka, K. Yamamoto, T. Hirayama, F. Sagane, M. Motoyama, Y. Iriyama, J. Power Sources 260 (2014) 292–298.

[199] K. Park, B.-C. Yu, J.-W. Jung, Y. Li, W. Zhou, H. Gao, S. Son, J.B. Goodenough, Chem. Mater. 28 (2016) 8051–8059.
[200] X. He, Y. Zhu, Y. Mo, Nat. Commun. 8 (2017) 15893.
[201] Y. Seino, T. Ota, K. Takada, A. Hayashi, M. Tatsumisago, Energy Environ. Sci. 7 (2014) 627–631.
[202] Y. Onodera, K. Mori, T. Otomo, A.C. Hannon, S. Kohara, K. Itoh, M. Sugiyama, T. Fukunaga, J. Phys. Soc. Jpn. 79 (2010) 87–89.
[203] H. Yamane, M. Shibata, Y. Shimane, T. Junke, Y. Seino, S. Adams, K. Minami, A. Hayashi, M. Tatsumisago, Solid State Ion. 178 (2007) 1163–1167.
[204] R. Kanno, M. Murayama, J. Electrochem. Soc. 148 (2001) A742–A746.
[205] M. Murayama, R. Kanno, M. Irie, S. Ito, T. Hata, N. Sonoyama, Y. Kawamoto, J. Solid State Chem. 168 (2002) 140–148.
[206] A. Martínez-Juárez, C. Pecharromán, J.E. Iglesias, J.M. Rojo, J. Phys. Chem. B 102 (1998) 372–375.
[207] J. Awaka, N. Kijima, H. Hayakawa, J. Akimoto, J. Solid State Chem. 182 (2009) 2046–2052.
[208] R. Murugan, V. Thangadurai, W. Weppner, Angew. Chem. Int. Ed. 46 (2007) 7778–7781.
[209] D. Rettenwander, C.A. Geiger, M. Tribus, P. Tropper, G. Amthauer, Inorg. Chem. 53 (2014) 6264–6269.
[210] C. Deviannapoorani, L. Dhivya, S. Ramakumar, R. Murugan, J. Power Sources 240 (2013) 18–25.
[211] R. Murugan, S. Ramakumar, N. Janani, Electrochem. Commun. 13 (2011) 1373–1375.
[212] L. Dhivya, N. Janani, B. Palanivel, R. Murugan, AIP Adv. 3 (2013) 279–287.
[213] S. Ramakumar, L. Satyanarayana, S.V. Manorama, R. Murugan, Phys. Chem. Chem. Phys. 15 (2013) 11327–11338.
[214] X. Yao, N. Huang, F. Han, Q. Zhang, H. Wan, J.P. Mwizerwa, C. Wang, X. Xu, Adv. Energy Mater., p. 1602923.
[215] W.J. Li, M. Hirayama, K. Suzuki, R. Kanno, Solid State Ion. 285 (2016) 136–142.
[216] H. Morimoto, H. Awano, J. Terashima, Y. Shindo, S. Nakanishi, N. Ito, K. Ishikawa, S.-i Tobishima, J. Power Sources 240 (2013) 636–643.
[217] Y. Li, W. Zhou, X. Chen, X. Lü, Z. Cui, S. Xin, L. Xue, Q. Jia, J.B. Goodenough, Proc. Natl. Acad. Sci. 113 (2016) 13313–13317.
[218] W. Zhou, S. Wang, Y. Li, S. Xin, A. Manthiram, J.B. Goodenough, J. Am. Chem. Soc. 138 (2016) 9385–9388.
[219] M. Kotobuki, Y. Suzuki, H. Munakata, K. Kanamura, Y. Sato, K. Yamamoto, T. Yoshida, J. Electrochem. Soc. 157 (2010) A493–A498.
[220] X. Lu, G. Wu, J.W. Howard, A. Chen, Y. Zhao, L.L. Daemen, Q. Jia, Chem. Commun. 50 (2014) 11520–11522.
[221] C.-W. Ahn, J.-J. Choi, J. Ryu, B.-D. Hahn, J.-W. Kim, W.-H. Yoon, J.-H. Choi, J.-S. Lee, D.-S. Park, J. Power Sources 272 (2014) 554–558.
[222] Y. Chen, L. Cai, Z. Liu, C.R.D. Cruz, C. Liang, K. An, Appl. Phys. Lett. 107 (2015) 621.